INL/JOU-24-80825-Revision-0

Evolution of dislocation loops in irradiated a-Uranium: An 1 atomistically-informed cluster dynamics investigation

May 2024

Sanjoy Kumar Mazumder, Tiankai Yao, Anter El-Azab

Changing the World's Energy Future

INL is a U.S. Department of Energy National Laboratory operated by Battelle Energy Alliance, LLC

INL/JOU-24-80825-Revision-0

Evolution of dislocation loops in irradiated a-Uranium: An 1 atomistically-informed cluster dynamics investigation

Sanjoy Kumar Mazumder, Tiankai Yao, Anter El-Azab

May 2024

Idaho National Laboratory
Idaho Falls, Idaho 83415

http://www.inl.gov

Prepared for the
U.S. Department of Energy
Under DOE Idaho Operations Office
Contract DE-AC07-05ID14517

Evolution of dislocation loops in irradiated α-Uranium: An atomistically-informed cluster dynamics investigation

Sanjoy Kumar Mazumder [a, *], Tiankai Yao [b] and

Anter El-Azab [a]

[a] School of Materials Engineering, Purdue University, West Lafayette, IN 47906, USA

[b] Idaho National Laboratory, Idaho Falls, ID 83415, USA

Abstract

An atomistically-informed mean field cluster dynamics model has been developed to investigate the nucleation and growth of prismatic loops in irradiated α-Uranium. TEM analysis of neutron irradiated α-Uranium shows the evolution of self-interstitial atom and vacancy loops on (010) and (100) crystallographic planes, respectively, resulting in an anisotropic lattice swelling of its face-centered orthorhombic crystal. To provide model parameters, the crystallography of loops and the binding energy of point defects to these loops were studied using an angular dependent EAM potential and classical molecular dynamics (MD) simulations. Furthermore, using the bond-boost hyperdynamics method, the anisotropic diffusion of interstitials and vacancies in α-Uranium was investigated. The mechanisms of point defect diffusion and the associated migration energies were reported and compared with previous DFT studies. The energetics and kinetic quantities mentioned above were used in the cluster dynamics model to predict the cluster density as a function of dose rate, dose and temperature and the results were compared to the reported neutron irradiation experiments. The model predictions reveal an accumulation of small sized vacancy loops along

with a population of large and growing self-interstitial loops, which closely corresponds to the TEM observations.

1. Introduction

Metallic uranium (U) and U alloys, such as U-Zr, U-Pu-Zr and U-Mo, are proposed as fuel forms for Generation IV fast reactors due to their superior thermal conductivity and higher fissile atom density as compared to oxide fuels [1]. At small alloying element content, the base fuel matrix has an orthorhombic crystal structure below 940 K and is named as α-U, an important allotrope of pure uranium. Despite its superior thermal properties, α-U suffers radiation induced microstructural changes and anisotropic swelling. When irradiated at ~ 150 °C, single crystals of α-U showed elongation along [010] crystallographic direction, contraction along [100] at a rate similar to the growth along [010], and no change along [001] axis [2]. In order to support U metallic fuel development, it is important to understand the anisotropic swelling mechanisms in α-U and quantify swelling rate along different crystallographic directions.

Several mechanisms have been proposed to explain this characteristic dimensional instability observed in α-U. Seigle and Opinsky [3] proposed that the anisotropic diffusion of lattice point defects, i.e., interstitials and vacancies generated during irradiation, results in this dimensional instability. The interstitials and vacancies diffuse preferably along [010] and [100] directions respectively. As the interstitials diffuse and add to the lattice, the vacancies diffuse and get absorbed at the grain boundaries and free surfaces. An unbalanced flux of the lattice point defects leads to an observable extension and contraction along [010] and [100], respectively. The proposed mechanism is similar to the theory of Nabarro [4]**,** which explains the observed changes in the dimension of metals, due to diffusion of vacancies between one free surface to the other, under applied external stress. Buckley [5] proposed another mechanism which is based on the anisotropic condensation of irradiation induced point defects, i.e., vacancies and interstitials, into planar clusters or dislocation loops. Clustering of interstitial loops on (010) planes and their subsequent

coarsening on prolonged irradiation leads to an addition of crystallographic planes along (010). This results in an extension of the crystal along [010]. Similarly, planar vacancy clusters preferentially evolve on (100) which eventually coarsen and remove crystallographic planes, contracting the α-U single crystal along [100]. Hudson et al. [6] reported the presence of (100) interstitial loops and (010) vacancy loops from the TEM observations of neutron irradiated α-U. At high irradiation doses, coalescence of these loops due to elastic interactions on their respective planes result in the change of single crystal dimensions as proposed by Buckley [5].

The mechanism of defect cluster accumulation on respective crystallographic planes, as hypothesized by Buckley [5] and confirmed from the experimental observations of Hudson et al. [6], provides a framework to systematically investigate and quantify the progress of damage in α-U upon irradiation. It is primarily governed by the nucleation and growth of point defect clusters, i.e., self-interstitial atom (SIA) and vacancy loops with irradiation dose. Cluster dynamics (CD), an approach based on chemical reaction rate theory [7, 8], has been widely used to study the evolution of irradiation-induced defect clusters in different materials like Fe [8, 9], stainless steel [10, 11], Zr [12] and oxide fuels [13, 14]. It uses a mean field approximation (MFA) to define rate equations for the evolution of SIA and vacancy clusters, of varying sizes, with dose. It assumes that point defects, i.e., SIA and vacancy are generated in the displacement cascade as Frenkel pairs, which migrate to and get absorbed by the existing clusters. For instance, a cluster having n SIAs can grow by absorbing an SIA to form a $(n+1)$ cluster. The n-sized SIA cluster can also shrink by absorbing a vacancy or emitting an SIA to form a $(n-1)$ cluster. Similarly, the vacancy clusters grow by absorption of vacancies and shrink by the absorption and emission of an SIA and vacancy, respectively. Each interaction mentioned above is associated with a rate constant that governs their kinetics. Finally, the rate of accumulation of SIA and vacancy clusters is obtained as

an aggregate of reaction rates for each interaction that the cluster is associated with. Thus, the CD model is a system of coupled ordinary differential equations (ODEs), each representing the accumulation rate of a specific sized cluster. Solution of the CD model gives the evolution of varying sized cluster population, with irradiation dose. An accurate prediction of the vacancy and SIA loop population would help to approximately estimate the anisotropic swelling in α-U, on irradiation.

The mechanism of dimensional instability in irradiated α-U proposed by Seigle and Opinsky [3] is driven by the anisotropic diffusion of SIA and vacancies along [010] and [100] crystallographic directions, respectively. Based on a theoretical analysis of α-U lattice, the ratio of diffusion coefficients for vacancies and SIAs along [100], [010] and [001] was calculated to be $1: 0: 0.8$ and $0.9: 0.9: 1$, respectively [3]. Experimental analysis of U self-diffusion in α-U reveals a vacancy exchange mechanism which is highly anisotropic [15, 16]. Vacancy self-diffusion is much easier in the corrugated (010) planes as compared to self-diffusion out of the planes, i.e., along [010] direction. Also, the self-diffusivity along [100] and [001], in the (010) corrugated planes of α-U, is almost similar. Although the experimentally obtained self-diffusivity of U migration is important evidence of the effect of crystal anisotropy on the diffusion properties of α-U, it does not infer anything about the individual point defect diffusivities. Huang et al. [17] computed the migration energy of both vacancies and SIAs along the three crystallographic directions using the climbing image nudged elastic band (CI-NEB) method in DFT. The vacancy migration energy was reported to be highly anisotropic, whereas the SIA migration energy was almost isotropic. Beeler et al. [18] used classical MD simulations, with the angular-dependent EAM interatomic potential by Starikov et al. [19], to compute the diffusivity of SIA and vacancies, without a detailed analysis on the anisotropic behavior of diffusion. Similarly, Wang et al. [20] have recently computed the

diffusivity of point defects along the different crystallographic directions in α-U using MD simulations with the EAM (ADP) potential by Starikov et al. [19]. They observed anisotropy in the diffusivity of SIA and vacancies, the migration energies of which varied significantly from the DFT predictions by Huang et al. [17]. Also, an analysis on the mechanism of point defect migration, leading to their anisotropic diffusion, needs to be discussed. Thus, it is required to further study the anisotropic diffusion of point defects in α-U. Also, the point defect diffusivities are critical parameters for the CD model.

In this work, we have investigated the evolution of irradiation induced SIA and vacancy loops in α-U using an atomistically-informed CD model. First, we have comprehensively discussed the crystallography of point defects and the SIA and vacancy loops that have been reported in the experimental literature. This helps us take a detailed look into the possible crystal structure of defect clusters and utilize our combined atomistic and CD approach to examine the evolution of the same, thus inferring the likelihood of any defect to be observed in actual irradiation conditions. Next, we have discussed the CD framework and the parameters of the model required to predict defect accumulation under irradiation. The cluster energetics discussed in the next section is an important parameter of the CD model and plays a significant role in the analysis of defect clusters that can exist in the irradiated matrix. The following section gives a detailed analysis of the mobility of point defects, U_i and V_U, in α-U using bond-boost hyperdynamics. The objective of this section is to understand the mechanisms of point defect diffusion and investigate any anisotropy in their migration, due to different mechanisms. The point defect diffusivities are also crucial parameters of the CD model which govern the kinetics of the cluster evolution phenomenon. Finally, the computed parameters have been used in the CD model to predict the progress of defect loop accumulation, of different types, with dose. The CD predictions have been

compared with the TEM observed evolution of defect clusters by Hudson et al. [6] and the strength and the limitations of the atomistically informed CD model has been discussed.

2.The cluster dynamics framework

2.1. The crystallography of SIA and vacancy loops in neutron irradiated α-U

α-U has a face-centered orthorhombic structure with densely packed corrugated (010) planes stacked along the [010] direction [17, 1] as shown in Fig. 1 and 2(a). The lattice parameters of the orthorhombic unit cell are 2.8537, 5.8695 and 4.9548 Å along [100], [010] and [001] respectively [21]. The possible self-interstitial sites in the structure of α-U has been demonstrated by Huang et al. [17], i.e., the tetrahedral and pentahedral pyramidal sites. The pentahedral site is formed by four atoms on a (010) corrugated plane along with a nearest-neighbor atom on the next (010) plane as shown in Fig. 2(b). The tetrahedral site is located adjacent to the pentahedral site, shown in Fig. 2(b), and is surrounded by two closed packed atoms each, from consecutive (010) planes. The

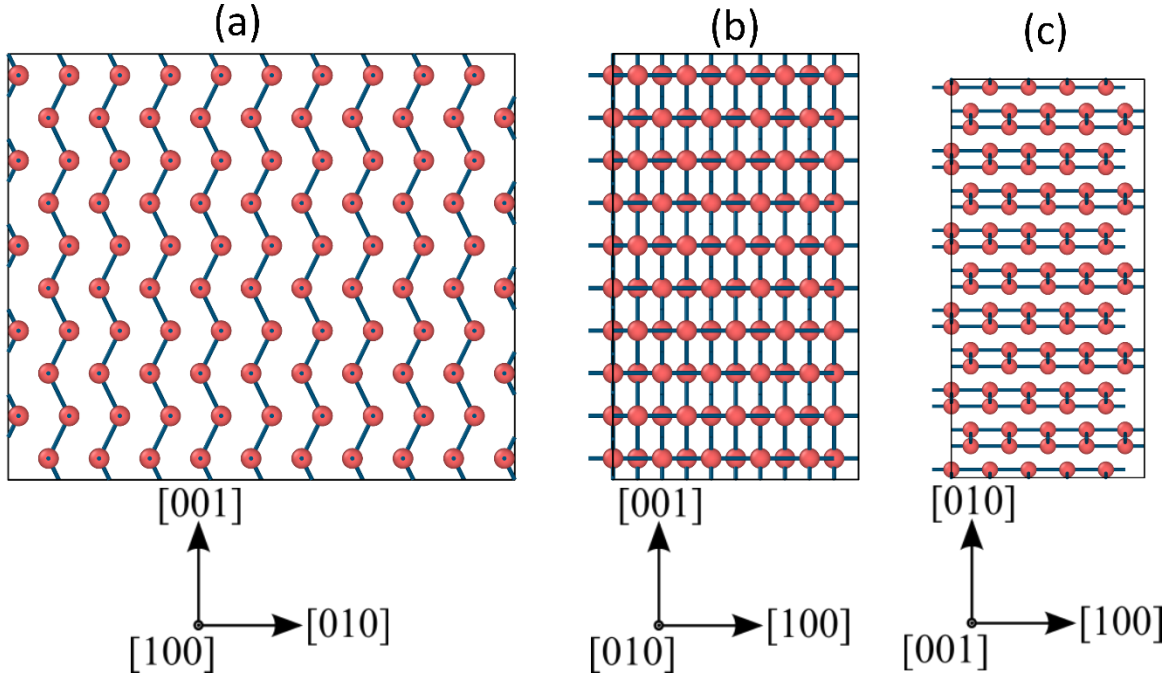

Figure 1. The face-centered orthorhombic crystal structure of α-U viewed along (a) [100] (b) [010] and (c) [001] directions.

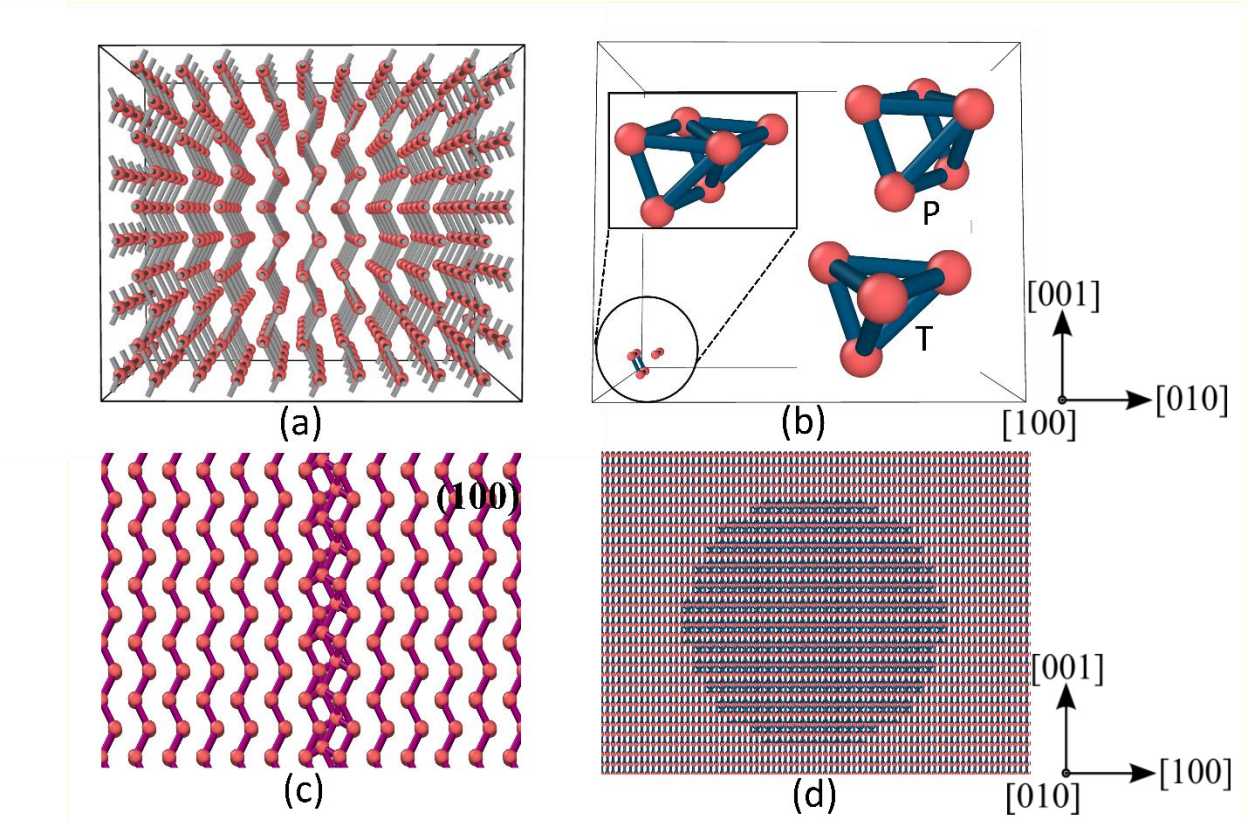

Figure 2. (a) Stacking of (010) corrugated planes in the orthorhombic structure of α-U. (b) Adjacent tetrahedral and pentahedral pyramidal voids, marked as T and P respectively, taken from the α-U structure in (a) (enlarged in the inset). An SIA loop is created by populating U_i at the pentahedral voids. (c) (100) and (d) (010) views of the SIA loop.

different types of loops reported by Hudson [22, 6] in neutron irradiated α-U are the $a[100](100)$ vacancy loops and the SIA loops lying on (010) planes with a Burgers vector $\frac{1}{2}\sqrt{a^2+b^2}\,[\bar{1}\bar{1}0]$, where a, b and c indicate the lattice parameter of α-U along [100], [010] and [001] respectively. These are prismatic loops characterized by a Burgers vector that lies out of the loop plane. The (010) crystallographic planes in α-U have a ABAB stacking sequence along [010] with the A and B layers displaced with respect to each other by $\frac{a}{2}\langle 100\rangle$. Introducing a layer of SIAs between two (010) planes, by populating them at the pentahedral sites, creates a stacking fault. The schematic of an SIA loop is shown in Fig. 2(c) and (d). The SIA loop assumes the configuration of a corrugated (010) plane and creates a stacking fault in the (010) layers. Li et al. [44] presents a

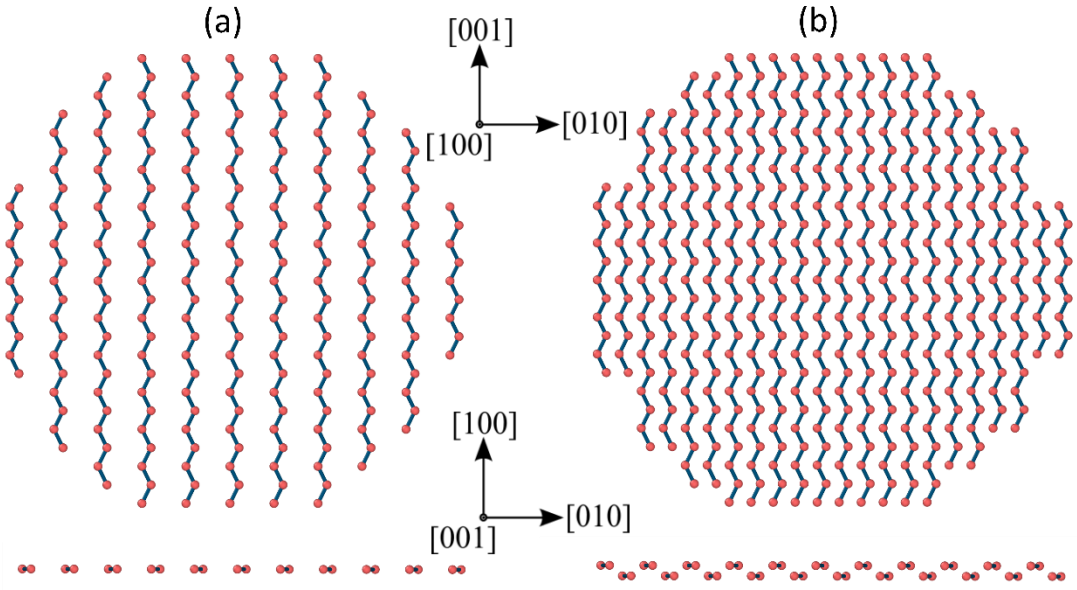

Figure 3. Configuration of prismatic vacancy loops on (100) planes of α-U with Burgers vector $a[100]$, (a) with and (b) without a stacking fault in the (100) planes.

similar configuration of the SIA prismatic loops but does not clearly explain the crystallography. The prismatic vacancy loops, on the other hand, form by the condensation of vacancies on a (100) plane, with a Burgers vector $a[100]$, normal to the plane of the loop. The configuration of (100) planes has been shown in Fig. 1(a). The stacking sequence of the (100) planes, in α-U, is ABAB along $[100]$ where the A and B layers are displaced with respect to each other by $\frac{b}{2}\langle 010\rangle$. Thus, the formation of a prismatic vacancy loop can create a stacking fault ABABBABA in the sequence of (100) planes if the condensation of vacancies take place on a single A plane. The condensation of vacancies on both consecutive A and B planes would result in a prismatic loop without a stacking fault. The schematic of both the vacancy loops have been shown in Fig. 3.

2.2. The cluster dynamics model

The cluster dynamics model used in this work to study the nucleation and growth of point defect clusters, is a set of coupled ODEs each representing the rate of accumulation of individual clusters

in the irradiated α-U matrix. Thus, the evolution of n-sized $(n > 2)$, SIA and vacancy cluster densities, denoted by $C_{n\mathrm{i}}$ and $C_{n\mathrm{v}}$ respectively, is described by [8]:

$$\frac{\mathrm{d}C_{n\mathrm{i}}}{\mathrm{d}t} = \left(\beta^{\mathrm{i}}_{(n-1)\mathrm{i}}C_{1\mathrm{i}}\right)C_{(n-1)\mathrm{i}} + \left(\beta^{\mathrm{v}}_{(n+1)\mathrm{i}}C_{1\mathrm{v}} + \alpha^{\mathrm{i}}_{(n+1)\mathrm{i}}\right)C_{(n+1)\mathrm{i}} - \left(\alpha^{\mathrm{i}}_{n\mathrm{i}} + \beta^{\mathrm{v}}_{n\mathrm{i}}C_{1\mathrm{v}} + \beta^{\mathrm{i}}_{n\mathrm{i}}C_{1\mathrm{i}}\right)C_{n\mathrm{i}}, \quad (1)$$

$$\frac{\mathrm{d}C_{n\mathrm{v}}}{\mathrm{d}t} = \left(\beta^{\mathrm{v}}_{(n-1)\mathrm{v}}C_{1\mathrm{v}}\right)C_{(n-1)\mathrm{v}} + \left(\beta^{\mathrm{i}}_{(n+1)\mathrm{v}}C_{1\mathrm{i}} + \alpha^{\mathrm{v}}_{(n+1)\mathrm{v}}\right)C_{(n+1)\mathrm{v}} - \left(\alpha^{\mathrm{v}}_{n\mathrm{v}} + \beta^{\mathrm{i}}_{n\mathrm{v}}C_{1\mathrm{i}} + \beta^{\mathrm{v}}_{n\mathrm{v}}C_{1\mathrm{v}}\right)C_{n\mathrm{v}}, \quad (2)$$

where the first term in Eq. (1) denotes the absorption of a $\mathrm{U_i}$ by a $(n-1)$i SIA cluster to form a ni cluster, the rate of which is determined by the coefficient of absorption, $\beta^{\mathrm{i}}_{(n-1)\mathrm{i}}$, the density of $\mathrm{U_i}$, $C_{1\mathrm{i}}$, and $(n-1)$i SIA clusters, $C_{(n-1)\mathrm{i}}$. The second and the third terms in Eq. (1) represents the rate of absorption of vacancies, $\mathrm{V_U}$, and the emission of $\mathrm{U_i}$ respectively, by $(n+1)$i SIA clusters resulting in the formation of ni clusters. The rate coefficient for $\mathrm{V_U}$ absorption and $\mathrm{U_i}$ emission by SIA clusters is denoted by $\beta^{\mathrm{v}}_{n\mathrm{i}}$ and $\alpha^{\mathrm{i}}_{n\mathrm{i}}$. The last three terms in Eq. (1) stands for the depletion in the density of ni clusters by absorption and emission of point defects. The rate of vacancy cluster accumulation is given similarly by Eq. (2). The equations governing the evolution of $C_{n\mathrm{i}}$ and $C_{n\mathrm{v}}$ is coupled with the equations for the rate of accumulation of $\mathrm{U_i}$, $\mathrm{V_U}$ and SIA and vacancy dimers $(n = 2)$, i.e., $\mathrm{U_i}$-$\mathrm{U_i}$ and $\mathrm{V_U}$-$\mathrm{V_U}$ given by:

$$\frac{\mathrm{d}C_{2\mathrm{i}}}{\mathrm{d}t} = 2\beta^{\mathrm{i}}_{1\mathrm{i}}C^2_{1\mathrm{i}} - 2\alpha^{\mathrm{i}}_{2\mathrm{i}}C_{2\mathrm{i}} - \beta^{\mathrm{i}}_{2\mathrm{i}}C_{1\mathrm{i}}C_{2\mathrm{i}} + \alpha^{\mathrm{i}}_{3\mathrm{i}}C_{3\mathrm{i}} - \beta^{\mathrm{v}}_{2\mathrm{i}}C_{1\mathrm{v}}C_{2\mathrm{i}} + \beta^{\mathrm{v}}_{3\mathrm{i}}C_{1\mathrm{v}}C_{3\mathrm{i}}, \quad (3)$$

$$\frac{\mathrm{d}C_{2\mathrm{v}}}{\mathrm{d}t} = 2\beta^{\mathrm{v}}_{1\mathrm{v}}C^2_{1\mathrm{v}} - 2\alpha^{\mathrm{v}}_{2\mathrm{v}}C_{2\mathrm{v}} - \beta^{\mathrm{v}}_{2\mathrm{v}}C_{1\mathrm{v}}C_{2\mathrm{v}} + \alpha^{\mathrm{v}}_{3\mathrm{v}}C_{3\mathrm{v}} - \beta^{\mathrm{i}}_{2\mathrm{v}}C_{1\mathrm{i}}C_{2\mathrm{v}} + \beta^{\mathrm{i}}_{3\mathrm{v}}C_{1\mathrm{i}}C_{3\mathrm{v}}, \quad (4)$$

$$\frac{\mathrm{d}C_{1\mathrm{i}}}{\mathrm{d}t} = G_{1\mathrm{i}} - R_{\mathrm{iv}}C_{1\mathrm{i}}C_{1\mathrm{v}} - 4\beta^{\mathrm{i}}_{1\mathrm{i}}C^2_{1\mathrm{i}} + 4\alpha^{\mathrm{i}}_{2\mathrm{i}}C_{2\mathrm{i}} + \beta^{\mathrm{v}}_{2\mathrm{i}}C_{1\mathrm{v}}C_{2\mathrm{i}} - C_{1\mathrm{i}}\sum_{n\geq 2}\beta^{\mathrm{i}}_{n\mathrm{i}}C_{n\mathrm{i}} + \sum_{n\geq 3}\alpha^{\mathrm{i}}_{n\mathrm{i}}C_{n\mathrm{i}} - C_{1\mathrm{i}}\sum_{n\geq 2}\beta^{\mathrm{i}}_{n\mathrm{v}}C_{n\mathrm{v}}, \quad (5)$$

$$\frac{\mathrm{d}C_{1\mathrm{v}}}{\mathrm{d}t} = G_{1\mathrm{v}} - R_{\mathrm{iv}}C_{1\mathrm{i}}C_{1\mathrm{v}} - 4\beta^{\mathrm{v}}_{1\mathrm{v}}C^2_{1\mathrm{v}} + 4\alpha^{\mathrm{v}}_{2\mathrm{v}}C_{2\mathrm{v}} + \beta^{\mathrm{i}}_{2\mathrm{v}}C_{1\mathrm{i}}C_{2\mathrm{v}} - C_{1\mathrm{v}}\sum_{n\geq 2}\beta^{\mathrm{v}}_{n\mathrm{v}}C_{n\mathrm{v}} + \sum_{n\geq 3}\alpha^{\mathrm{v}}_{n\mathrm{v}}C_{n\mathrm{v}} - C_{1\mathrm{v}}\sum_{n\geq 2}\beta^{\mathrm{v}}_{n\mathrm{i}}C_{n\mathrm{i}}. \quad (6)$$

In Eq. (5) and (6), $G_{1\mathrm{i}}$ and $G_{1\mathrm{v}}$ represents the rate of generation of U_i and V_U, respectively, by the atomic displacement events under irradiation. Considering the generation of monomers as Frenkel pairs, $G_{1\mathrm{i}}$ and $G_{1\mathrm{v}}$ should be equal. The rate of point defect depletion due to the recombination of U_i and V_U is given by the second term in Eq. (5) and (6). Also, the loss of mobile defects to the microstructural sinks like dislocations and grain boundaries have been neglected in the development of current CD model. The model is thus developed to study point-defect clustering in irradiated single crystals with low dislocation density. TEM analyses by Hudson and coworkers [6] report no difference in the size and density of dislocation loops at the grain interior and the boundary at a neutron irradiation dose of 0.5 dpa and 80°C. Also, any effect of dislocation sinks on point-defect clustering has not been particularly highlighted [6, 22]. Thus, the assumption of neglecting the effect of microstructural sinks in the CD model, although not accurate, is reasonable for comparing with the TEM observations [6, 22]. The solution of the coupled set of ODEs Eq. (1) through (6) gives the density evolution of SIA and vacancy prismatic loops of all sizes, with the progress of irradiation.

2.3. Cluster dynamics model parameters

The solution of the CD model mentioned above is dependent on the rate coefficients for individual interactions between defects. In this work, we have defined the reaction rate coefficients similar to the CD model presented by Duparc et al. [8]. The rate of SIA and vacancy recombination is given by the second term in Eq. (5) and (6) where R_{iv} is the coefficient of recombination,

$$R_{\mathrm{iv}} = 4\pi r_{\mathrm{iv}}\left(D_{\mathrm{U_i}} + D_{\mathrm{V_U}}\right). \tag{7}$$

This is a diffusion-controlled interaction where the diffusivity of interacting species, i.e., $D_{\mathrm{U_I}}$ and $D_{\mathrm{V_U}}$ govern the rate of reaction. Also, $r_{\mathrm{iv}}{\sim}2.5a$ is the radius of recombination, i.e., radius of the spherical volume surrounding a point defect within which the recombination with the opposite point defect occurs spontaneously and a is the lattice parameter. Similarly, the mobile point defects, i.e., $\mathrm{U_i}$ and $\mathrm{V_U}$, diffuse to the immobile clusters and gets absorbed, the rate-coefficient of which is defined as:

$$\beta_{n\mathrm{i}}^{S} = 2\pi R_{n\mathrm{i}} Z_{ni}^{S} D_S, \tag{8}$$

$$\beta_{n\mathrm{v}}^{S} = 2\pi R_{n\mathrm{v}} Z_{n\mathrm{v}}^{S} D_S, \tag{9}$$

where $S = \mathrm{U_i}$, $\mathrm{V_U}$ and ni, nv denote dislocation loops with n SIAs and vacancies respectively. $R_{n\mathrm{i}}$ and $R_{n\mathrm{v}}$ are the radii of SIA and vacancy loops respectively and $Z_{n\mathrm{i}}^{S}$, $Z_{n\mathrm{v}}^{S}$ indicate the bias factors, i.e., capture efficiency of SIA and vacancy loops towards individual point defects. The loop radii are given as:

$$R_{n\mathrm{i(v)}} = \left(\frac{n\Omega}{\pi b}\right)^{\frac{1}{2}}, \tag{10}$$

where b is the Burgers vector of SIA and vacancy dislocation loops and $\Omega \sim \frac{a^3}{4}$ is the atomic volume and is approximately equal to a quarter of the unit cell volume $\sim a^3$, as the effective number of atoms in α-U unit cell is 4. The bias factors are given by:

$$Z_{ni(v)}^{S} = Z_S^{d} + \frac{\left[\left(\frac{b}{8\pi a}\right)^{\frac{1}{2}} z_S - Z_S^{d}\right]}{n^{\frac{\gamma_S}{2}}}, \tag{11}$$

where Z_S^{d} denotes the bias of dislocation lines towards individual point defects which is 1 for U_i and 1.2 for V_U [8]. The factors $z_{U_i} = 42$, $z_{V_U} = 35$ and $\gamma_{U_i} = \gamma_{V_U} = 0.7$ are also defined similar to the CD model by Duparc et al. [8]. Finally, the rate coefficient of the emission of U_i and V_U from the SIA and vacancy loops respectively are expressed in the form:

$$\alpha_{ni}^{U_i} = \beta_{(n-1)i}^{U_i} \exp\left(-\frac{E_{ni}^{B}}{kT}\right), \tag{12}$$

$$\alpha_{nv}^{V_U} = \beta_{(n-1)v}^{V_U} \exp\left(-\frac{E_{nv}^{B}}{kT}\right), \tag{13}$$

where E_{ni}^{B} and E_{nv}^{B} are the binding energies of U_i and V_U to a $(n-1)$ SIA and vacancy loop respectively. The emission of point defects is governed by the kinetics of point defect migration and the energetics of loops with varying sizes. Thus, the important parameters used in the calculation of the rate coefficients in the CD model are the diffusivities of point defects, i.e., D_{U_i}, D_{V_U} and the binding energy of point defects to the defect clusters. The following section discusses in detail the calculation of these parameters using atomistic simulations.

3. Atomistic calculation of cluster dynamics model parameters

3.1. The binding energy of point defects to clusters

The binding energy of U_i and V_U to SIA and vacancy loops, respectively, corresponding to the definition of binding energy by Duparc et al. [8] for pure materials is:

$$E_{n\mathrm{i}}^{\mathrm{B}} = E_{\mathrm{U_i}}^{\mathrm{f}} - \left(E_{n\mathrm{i}}^{\mathrm{f}} - E_{(n-1)\mathrm{i}}^{\mathrm{f}}\right), \tag{14}$$

$$E_{n\mathrm{v}}^{\mathrm{B}} = E_{\mathrm{V_U}}^{\mathrm{f}} - \left(E_{n\mathrm{v}}^{\mathrm{f}} - E_{(n-1)\mathrm{v}}^{\mathrm{f}}\right), \tag{15}$$

where $E_{\mathrm{U_i}}^{\mathrm{f}}$ and $E_{\mathrm{V_U}}^{\mathrm{f}}$ are the formation energy of respective point defects whereas $E_{n\mathrm{i}}^{\mathrm{f}}$ and $E_{n\mathrm{v}}^{\mathrm{f}}$ denote the formation energy of SIA and vacancy loops respectively. Recent CD models by X.-Y. Liu et al. [48] and C. Matthews et al. [49, 50] define the driving force of a reaction as the associated change in free energy of the system. In our CD model, the binding energy of monomers to clusters, i.e., $E_{ni}^{\mathrm{B}}, E_{nv}^{\mathrm{B}}$, represent the driving force of the clustering phenomenon. In defining the binding energy, as shown in Eq. (14) and (15), contribution of the internal energy term has only been considered. Assuming that the clusters always adopt a closed packed configuration, change in entropy of the system associated with the binding of monomers has been neglected. Thus, we approximated the change in free energy of the system due to monomer-cluster interaction with the change in internal energy, i.e., $E_{ni}^{\mathrm{B}}, E_{nv}^{\mathrm{B}}$. The SIA and vacancy formation energies have been reported in literature using density functional theory (DFT), as well as classical molecular dynamics (MD) calculations with EAM [23, 24] and Angular Dependent EAM [19] or ADP interatomic potentials. A list of point defect formation energy values reported in literature is shown in Table. 1.

Table 1. The formation energy of point defects in α-U.

	DFT	MD
$E^{\mathrm{f}}_{\mathrm{U_i}}$	4.42 [17], 3.53 - 3.87 eV [25]	Temperature dependent 2.5 - 3.4 [18], 3.1 – 3.8 [28], 2.4 – 3.7 [20]
$E^{\mathrm{f}}_{\mathrm{V_U}}$	1.69 [17], 1.86 [26], 1.95 [27]	2.14 eV [24] Temperature dependent 1.4 – 1.9 [18], 1.1 – 2.0 [28], 1.4 – 1.7 [20]

In this work, we have computed the formation energy of SIA and vacancy loops, $E^{\mathrm{f}}_{n\mathrm{i}}$ and $E^{\mathrm{f}}_{n\mathrm{v}}$ respectively, using LAMMPS (https://www.lammps.org) [47], with the ADP interatomic potential by Starikov et al. [19]. In doing so, we have introduced the loop in a perfect α-U system with a dimension of $40 \times 20 \times 30$ unit cells along [100], [010] and [001] with 96000 atoms, as shown in Fig. 2(c), and minimized the internal energy of the system in LAMMPS, using conjugate gradient relaxation. The system was anisotropically relaxed along three crystallographic directions, while maintaining it orthogonal. Following energy minimization, the system was thermally equilibrated at a low temperature of 10 K and 0 bar pressure, in an NPT ensemble, for 60 ps. Thermal equilibration at a low (near 0 K) temperature relaxes the system properly and allows

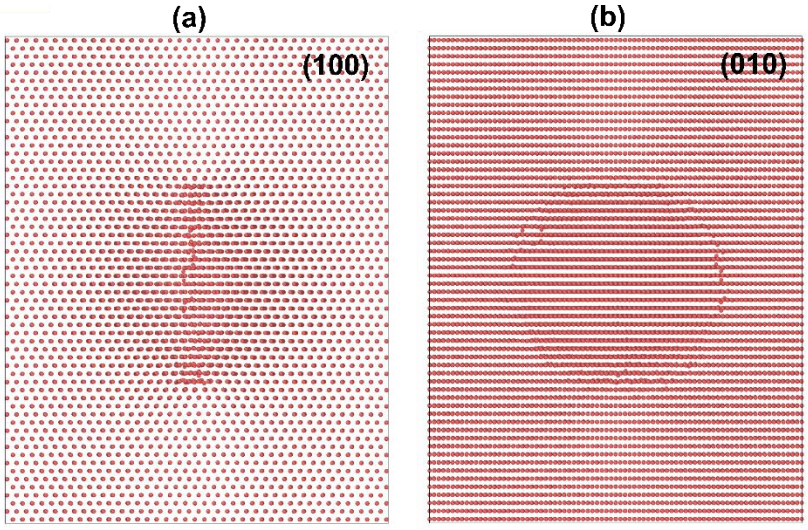

Figure 4(a) A (100) view of the distortion in crystallographic planes of α-U due to the presence of a SIA loop, after NPT equilibration at 10K and 0 bar. (b) A (010) view shows that the SIA loop relaxes reasonably well in between the (010) planes.

the loop to achieve a minimum energy configuration as shown in Fig. 4. Distortion of the crystallographic planes in a relaxed configuration of a system with SIA loop, is clearly visible. The SIA loop relaxes properly in between the (010) crystallographic planes as it becomes invisible in the (010) view of the orthorhombic crystal as shown in Fig. 4(b). Distortion of crystallographic planes in a system with vacancy loop after relaxation is not distinctly identifiable and hence not shown.

The internal energy of the system after equilibration is denoted as E_{Loop}. A defect-free perfect crystal of α-U having dimension $40 \times 20 \times 30$ unit cell is similarly relaxed and thermally equilibrated at 10 K and 0 bar pressure. The internal energy of the relaxed perfect system is denoted as E_{Perfect}. Thus, the formation energy of SIA and vacancy loops may be written as:

$$E^{\mathrm{f}}_{n\mathrm{i(v)}} = E_{\mathrm{Loop}} - E_{\mathrm{Perfect}} + n\mu_{\mathrm{i(v)}}, \tag{16}$$

where μ_{i} and μ_{v} are the changes in internal energy associated with introducing a lattice atom or a vacancy in a defect-free crystal. Equilibration at a low temperature, i.e., near 0 K, allows us to define μ_{i} and μ_{v} in terms of the internal energy per atom in a perfect crystal, i.e., $e = \frac{E_{\mathrm{Perfect}}}{N_{\mathrm{Perfect}}}$ where $N_{\mathrm{Perfect}} = 96000$ atoms, as:

$$\mu_{\mathrm{i}} = -e, \mu_{\mathrm{v}} = e. \tag{17}$$

This implies that the introduction of a lattice atom is associated with a negative change in the internal energy of the system due to the formation of new bonds, while a vacancy does the opposite. The formation energy of loops calculated using Eq. (16) is used to obtain the binding energy of point defects using Eq. (14) and (15).

The calculated formation energy of SIA loops and the binding energy of point defect is shown in Fig. 5(a). E_{ni}^{f} of very small loops have not been computed as they dissociate easily and hence difficult to identify after relaxing the system. The fitted plot of E_{ni}^{f}, calculated using LAMMPS, varies with $n^{0.7}$ which is similar to the variation with $n^{\frac{2}{3}}$ as reported by Soneda et al. [29] for SIA loops in α-Fe. This implies that for large n, the elastic energy contributes significantly to the loop formation energy [8]. According to Eq. (14) and (15), a positive value of point defect binding energy indicates a stable n-sized loop, the shrinking of which is energetically unfavorable. As observed in Fig. 5(b), energy associated with the emission of an SIA from an n-sized loop, E_{ni}^{B},

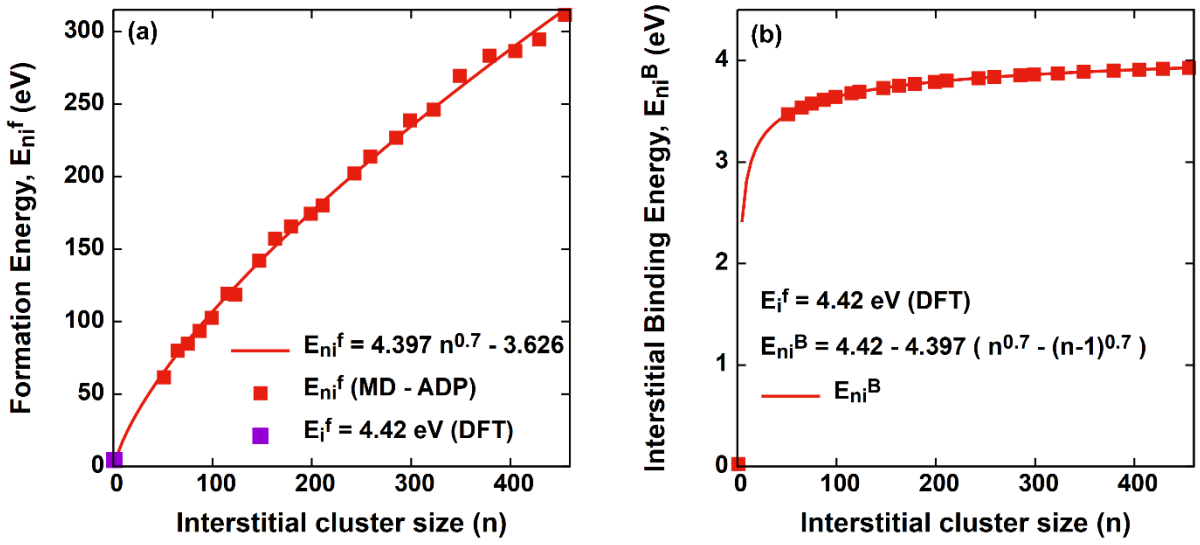

Figure 5. Plot of the (a) SIA loop formation energy, E_{ni}^{f}, calculated using MD and (b) binding energy of SIA to loops, E_{ni}^{B}, with loop size. The SIA formation energy, E_{i}^{f}, indicated in the plot is taken from the first-principles calculations performed by Huang et al. [17].

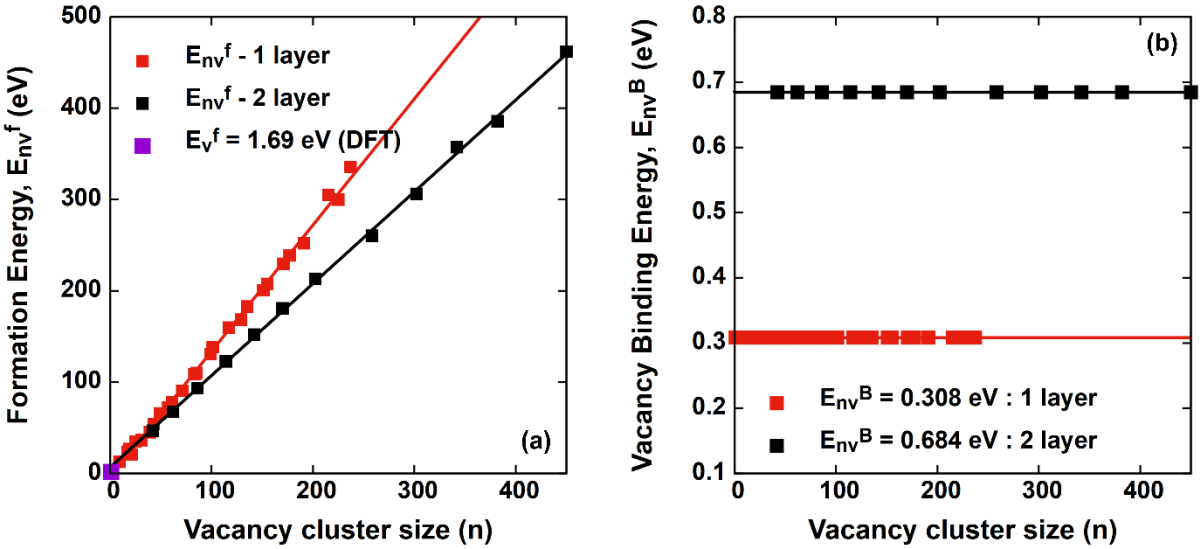

Figure 6. Plot of (a) vacancy loop formation energy, E_{nv}^f, with loop size n, calculated using MD and (b) the binding energy of vacancy to loops, E_{nv}^B, with loop size n. The vacancy formation energy, E_v^f, indicated in the plot is taken from the first-principle calculations performed by Huang et al. [17].

has lower positive values for small loops, making them more likely to dissociate. As loop size increases, E_{ni}^{B} increases and almost saturates with n. This indicates that the dissociation of larger SIA loops into a smaller loop and an SIA is energetically less favorable, the tendency of which becomes nearly similar for increasing loop sizes. The formation energy of vacancy loops has been computed similarly, as shown in Fig. 6(a). In Fig. 3, we have talked about single and double layered $a[100](100)$ vacancy prismatic loops associated with and without a stacking fault respectively. Fig. 6(a) shows the variation of E_{nv}^{f} with size, n, for both vacancy loops. Unlike the SIA loops, E_{nv}^{f} varies linearly with n which does not correspond to the variation of E_{nv}^{f} with $n^{\frac{2}{3}}$ as reported by Soneda et al. [29] for vacancy loops in α-Fe. This indicates that the energy of the stacking fault predominantly contributes to the loop formation energy [46], shown below:

$$E_{nv}^{\mathrm{f}} = 4\pi\gamma_{\mathrm{SF}}R_{nv}^2, \tag{18}$$

where γ_{SF} and $R_{n\mathrm{v}}$ are the stacking fault energy and vacancy loop radius respectively. Substituting $R_{n\mathrm{v}}$ from Eq. (10), we obtain:

$$E_{n\mathrm{v}}^{\mathrm{f}} = 4\pi\gamma_{\mathrm{SF}}\left(\frac{n\Omega}{\pi b}\right). \quad (19)$$

Also, the formation energy of single layered faulted loops is higher as compared to the double layered prismatic loops for the same loop size, n. This is because, the faulted area is larger for single layered loops for the same n. Thus, the energy of stacking fault plays a significant role in determining the energetics of vacancy loops. The binding energy of vacancy to loops computed using Eq. (15) is constant over all loop sizes, n, as shown in Fig. 6(b) which is a consequence of the linear variation of $E_{n\mathrm{v}}^{\mathrm{f}}$ with n. Also, $E_{n\mathrm{v}}^{\mathrm{B}}$ is greater for double layered prismatic vacancy loops as compared to single layered faulted loops, indicating that the former is more stable as compared to the latter.

3.2. The diffusivity of point defect in α-U

In this section, we discuss the diffusivity of $\mathrm{U_i}$ and $\mathrm{V_U}$ in α-U computed using accelerated molecular dynamics. Diffusion being a rare-event phenomenon is difficult to model using classical MD due to the limited timescale. Accelerated MD methods like temperature accelerated dynamics (TAD) [30, 31], bond-boost hyperdynamics [32, 33, 34] and parallel replica dynamics [35] are used to model long-time evolution of such atomic phenomenon while accurately accounting for the short-time processes. We have used bond-boost hyperdynamics [32] to compute SIA and vacancy diffusivities. TAD was avoided since it would require a high temperature, ~1000 K or above, which would result in a transformation of the U structure from face-centered orthorhombic, α, to body-centered tetragonal, β, at 935 K [36, 19].

3.2.1 Bond-boost hyperdynamics

In the general description of hyper-MD methods [33, 32], the rate of transition of a system with a point defect from one configuration to the other is obtained from the transition state theory (TST). A transition takes place from one minimum energy configuration to another across an energy barrier, also called a hypersurface. At a fixed temperature, the system is assumed to have properly equilibrated at the minimum energy configuration before its transition across the hypersurface. The rate of this transition, k^{TST}, is obtained as a canonical-ensemble average of the system velocity across this hypersurface. Addition of an empirical boost potential, ΔV, to the potential energy landscape of the system in the phase space, such that ΔV is zero at the hypersurface and non-zero positive everywhere else, the transition rate, k^{b}, is enhanced by a factor as shown below:

$$k^{\mathrm{b}} = k^{\mathrm{TST}}\langle \exp(\beta \Delta V)\rangle_{\mathrm{b}} \; ; \beta = \frac{1}{K_B T}, \tag{20}$$

where $\langle \exp(\beta \Delta V)\rangle_{\mathrm{b}}$, also known as the boost factor, is the canonical-ensemble average of $\exp(\beta \Delta V)$ over the boosted potential surface. The average escape time of the system from one minimum energy configuration, across the hypersurface, is also enhanced by the boost factor, i.e.,

$$\tau^{\mathrm{b}} = \tau^{\mathrm{TST}}\langle \exp(\beta \Delta V)\rangle_{\mathrm{b}}, \tag{21}$$

which increases the physical time over which the system evolves, from the actual simulation time, by the same factor. In the simplified bond-boost hyperdynamics demonstrated by Kim et al. [37], at any time the boost potential, shown in Eq. (20), is applied to one bond in the system, δV_i, between the atom, trying to undergo a transition from one minimum energy configuration to the other, and its nearest neighbor.

$$\delta V_i = \delta V(\epsilon_i) = \begin{cases} \Delta V^{\max}\left[1 - \left(\frac{\epsilon_i}{q}\right)^2\right], & |\epsilon_i| < q \\ 0, & |\epsilon_i| \geq q \end{cases}. \quad (22)$$

The relative distortion in the bond, ϵ_i, making the transition, is defined as:

$$\epsilon_i = \frac{\left[r_i - r_i^{\mathrm{eq}}\right]}{r_i^{\mathrm{eq}}}, \quad (23)$$

where r_i and r_i^{eq} indicate the instantaneous and equilibrium bond lengths respectively. The boost potential δV_i, is such that it is maximum, i.e., $\Delta V^{\max}$, when there is no distortion in the bond length and vanishes at a threshold value q. The potential is applied to a bond undergoing transition, as repulsive force, defined by Eq. (22), on the constituent atoms of the bond.

$$f_i = -\frac{\partial \Delta V(\epsilon_i)}{\partial \epsilon_i} = f(x) = \begin{cases} 2\Delta V^{\max}\epsilon_i/q^2, & |\epsilon_i| < q \\ 0, & |\epsilon_i| \geq q \end{cases}. \quad (24)$$

Thus, the boost potential helps an atom undergo transition from one equilibrium configuration to the other by the application of a repulsive force, in addition to the forces calculated from classical MD, which ceases to act as the threshold bond distortion, q, is reached. At this point, the system is believed to have transitioned across the hypersurface.

We have used LAMMPS [47] to implement this bond-boost hyperdynamics method for studying the migration of point defects in α-U. It is important to choose the threshold bond distortion, q, appropriately as it determines the location of hypersurface specific to the phenomenon under investigation. Also, the maximum bias potential, $\Delta V^{\max}$, should be on the scale of the natural energy barrier of the system [32]. We used an α-U simulation cell of dimension $8 \times 4 \times 4$ unit cells and 2940 U atoms and introduced U_i at a pentahedral pyramidical interstitial site as shown in Fig. 2(b) or a V_U at any lattice position. The system was relaxed anisotropically while maintaining it orthogonal, followed by equilibration at a constant temperature, T, with a Langevin thermostat,

in an NVE ensemble for 5 ns. Finally, we performed bond-boost hyperdynamics, for 10^5 timesteps, where a single pair of atoms is selected at every timestep and a global boost potential is applied. This accelerates the migration of point defects, thus allowing the sampling of diffusion events over long time.

For studying the diffusion of U_i and V_U, we have used a range of threshold bond distortion values, $q = \{0.3, 0.35, 0.4, 0.45\}$ among which a value of $q = 0.3$ was chosen to best obtain near linear mean squared displacement plots for diffusivity calculations. Since $\Delta V^{\max}$ needs to be in the scale of natural energy barriers of system [32], the hyperdynamics simulations were also performed for a range of $\Delta V^{\max} = \{0.1, 0.2, 0.3\}$, keeping in mind the reported values of $E^{\mathrm{m}}_{\mathrm{U_i}}$ and $E^{\mathrm{m}}_{\mathrm{V_U}}$ in literature as listed in Table. 2. The choice of a large $\Delta V^{\max}$ increases the boost factor which allows the diffusion events to happen easily. For U_i diffusion, increasing $\Delta V^{\max}$ effectively boosts the slow diffusion events at lower temperatures. A comparison of the boost factors at different temperatures, for U_i diffusion using $\Delta V^{\max} = 0.3$ eV, is shown in Fig. 8(d). On the other hand, for the same $\Delta V^{\max}$, diffusion of V_U is slightly boosted only at low diffusion temperatures, as shown in Fig. 9(c). At high temperatures, the boost potential nearly equals unity which implies that the events are frequent and does not need boosting. The diffusion of vacancies is not significantly boosted even with high $\Delta \mathrm{V}^{\max} = 0.4$ and 0.5 eV, as presented in the supplementary information.

Table 2. The diffusivity of point defects in α-U.

	E^{m}(eV)	D^{o} (cm^2/s)
U_i	DFT [17] $[100]0.22, [010]0.22, [001]0.19$ MD (ADP) [18] Isotropic 0.35 MD (ADP) [20]	MD (ADP) [18] Isotropic 2.172×10^{-3} MD (ADP) [20] $[100]6.23 \times 10^{-3}$ $[010]3.93 \times 10^{-3}$ $[001]4.96 \times 10^{-3}$

	[100]0.479, [010]0.413, [001]0.411 Isotropic 0.420 Hyperdynamics (This work) [100]0.505, [010]0.431, [001]0.319 Isotropic 0.337	Isotropic 1.259×10^{-2} Hyperdynamics (This work) [100]3.57×10^{-3} [010]2.41×10^{-3} [001]1.08×10^{-3} Isotropic 2.14×10^{-3}
V_U	DFT [17] [100]0.34, [010]1.24, [001]0.36 MD (ADP) [18] Isotropic 0.34 MD (ADP) [20] [100]0.455, [010]0.394, [001]0.419 Isotropic 0.434 Hyperdynamics (This work) [100]0.696, [001]0.433 Isotropic 0.572	MD (ADP) [18] Isotropic 1.148×10^{-3} MD (ADP) [20] [100]5.78×10^{-3} [010]1.99×10^{-4} [001]2.49×10^{-3} Isotropic 7.77×10^{-3} Hyperdynamics (This work) [100]2.85×10^{-1} [001]2.62×10^{-3} Isotropic 7.01×10^{-2}

The Wigner Seitz defect analysis modifier in OVITO visualization tool [38] helps identify the position of defects, at every 10^3 timesteps. In this work, we have performed a complete analysis of the point defect diffusivities, i.e., both the migration energy, E^{m}, and the diffusion pre-exponent, D^{o}. In order to do so, we have plotted the mean squared displacement, $\langle r^2 \rangle$, of the migrating point defects against time, t, the slope of which gives a measure of the diffusivity according to the Einstein's relation:

$$\langle r^2 \rangle = 6Dt. \tag{25}$$

We have tried to capture the anisotropy in diffusion by modifying Eq. (23) as:

$$\langle (\Delta x)^2 \rangle + \langle (\Delta \mathrm{y})^2 \rangle + \langle (\Delta \mathrm{z})^2 \rangle = 6\big(D_x + D_y + D_z\big)t, \tag{26}$$

where $\langle (\Delta x)^2 \rangle$, $\langle (\Delta y)^2 \rangle$ and $\langle (\Delta z)^2 \rangle$ are the mean squared displacements and D_x, D_y and D_z are the diffusivities of the migrating point defect along [100], [010] and [001] crystallographic directions respectively. The hyper-MD runs were performed at 8 different temperatures and

repeated 10 times at each temperature. The diffusivities were obtained as an average of the slope of the mean squared displacement plots from different runs at each temperature as shown in Fig. 8.

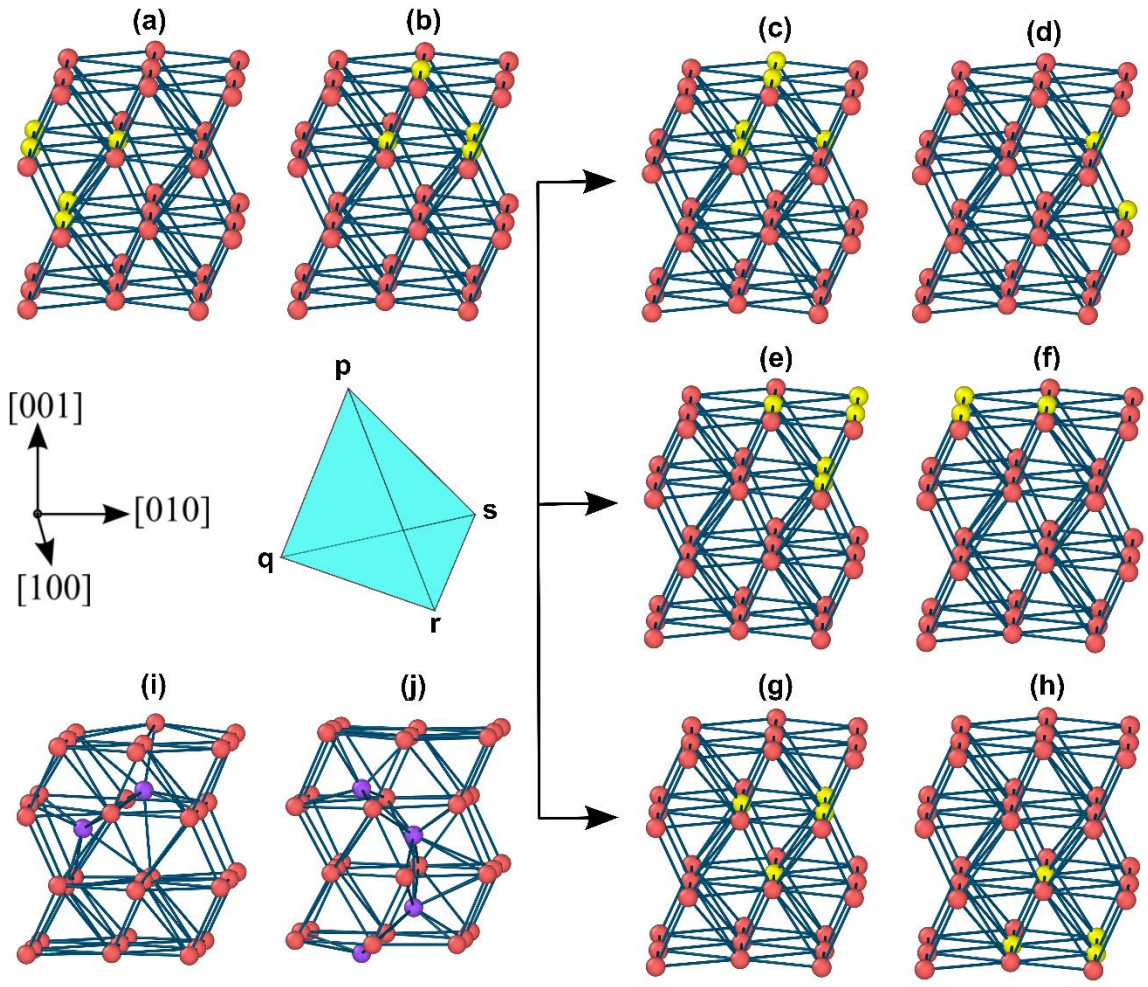

Figure 7. Migration of U_i in an α-U unit cell. A pentahedral pyramidal site for U_i has been highlighted with yellow in (a). The occupied pentahedral site in a dumbbell SIA configuration is shown, marked with blue, in (i). (b) Highlighted atoms show a tetrahedral site into which the lattice U atom is kicked out by U_i via an interstitialcy mechanism, giving the new position of U_i. Schematic of the tetrahedral site is shown by the tetrahedron 'pqrs'. The new U_i can migrate via three different mechanisms. **First mechanism:** (c) New U_i migrates to an adjacent pentahedral site (highlighted) across the face 'pqs' of the tetrahedron. (d) Kicks out, via interstitialcy mechanism, the lattice U atom at the apex of pentahedral site to a tetrahedral site out of the unit cell, two atoms of which have been highlighted. **Second mechanism:** (e) New U_i migrates to an adjacent pentahedral site (highlighted) across the face 'prs' of the tetrahedron. (f) Kicks out, via interstitialcy mechanism, the lattice U atom at the apex of pentahedral site to a tetrahedral site out of the unit cell, three atoms of which have been highlighted. **Third mechanism:** (g) New U_i migrates to an adjacent tetrahedral site (highlighted) across the face 'qrs' of the tetrahedron and (h) shares a lattice site with an U atom at the apex of the tetrahedral site, which partly occupies another tetrahedral site (highlighted). (j) The SIA configuration, marked in blue, that results from the third mechanism, is also called a three-site interstitial [17].

1

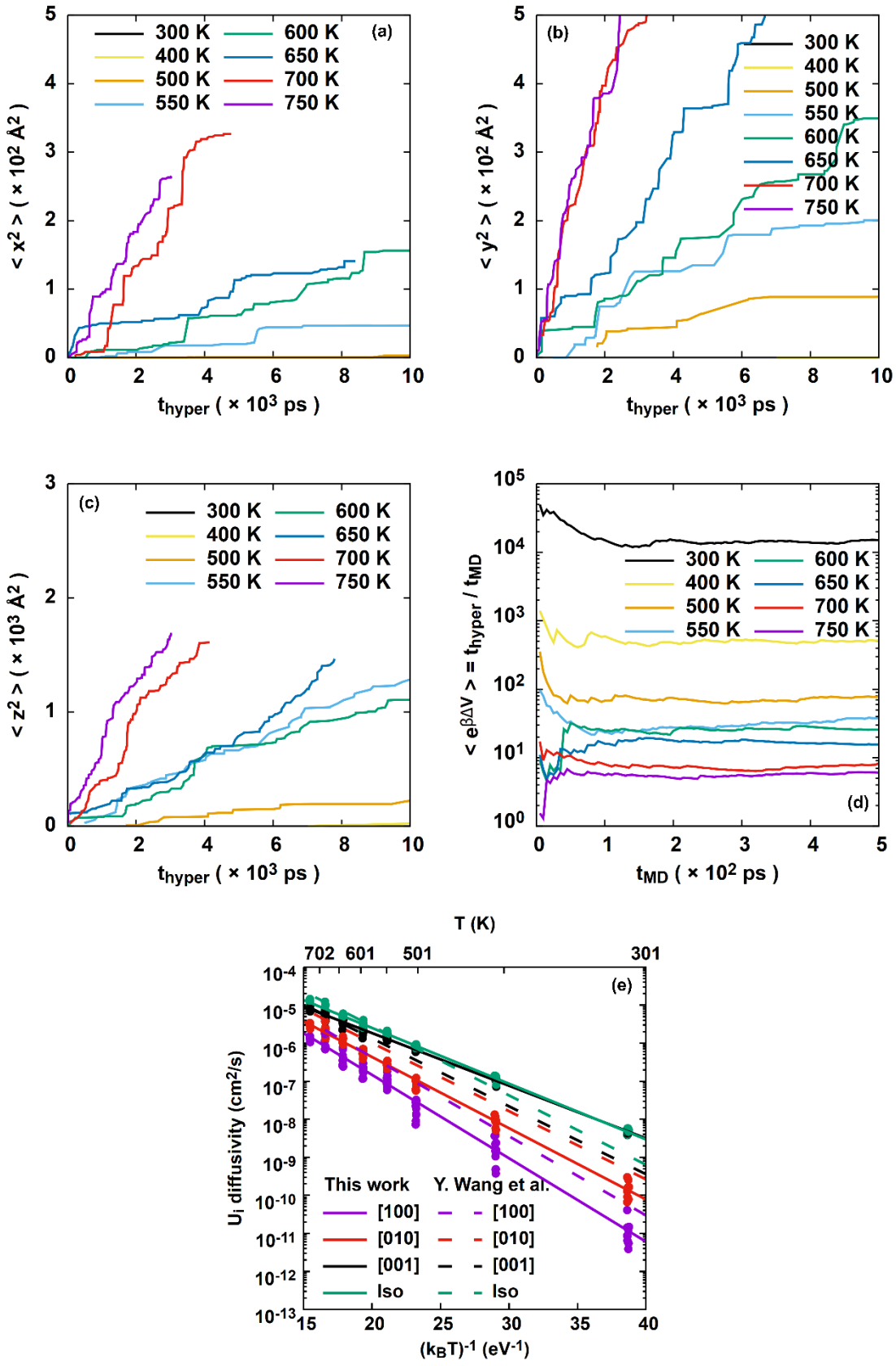
(a)
300 K
400 K
500 K
550 K
600 K
650 K
700 K
750 K
< x² > (× 10² Å²)
t_hyper (× 10³ ps)
(b)
< y² > (× 10² Å²)
t_hyper (× 10³ ps)
(c)
< z² > (× 10³ Å²)
t_hyper (× 10³ ps)
(d)
< e^βΔV > = t_hyper / t_MD
t_MD (× 10² ps)
T (K)
702 601 501 301
(e)
U_i diffusivity (cm²/s)
This work
Y. Wang et al.
[100]
[010]
[001]
Iso
(k_B T)^-1 (eV^-1)

1

Figure 8. Mean squared displacement (MSD) plots at different temperatures for U_i diffusion along (a) [100], (b) [010] and (c) [001] using $\Delta V^{max} = 0.3\ eV$. (d) A comparison of the boost factors for U_i diffusion at different temperatures. (e) D_{U_i} along different crystallographic directions. The plot shows a comparison of D_x, D_y and D_z in terms of the E^m and D^o along [100], [010] and [001] respectively. The computed diffusivity values have been compared with the diffusivity values obtained by Wang et al. [20] using MD.

3.2.2 Diffusivity of U_i

The diffusivity of U_i seems to be the highest along [001], closely followed by the diffusivities along the other two crystallographic axes. This is evident from the mean squared displacement plots shown in Fig. 8(a), (b) and (c). The distance covered by U_i is an order of magnitude greater along [001] as compared to along [100] and [010]. Though there is a significant scatter in the computed diffusivities along different directions, shown in Fig. 8(e), the anisotropy is apparent at nearly all temperature. U_i occupies a pentahedral site in a dumbbell configuration with a lattice U atom at the apex, which partly occupies an adjacent tetrahedral site. Diffusion of U_i in α-U follows a combination of interstitialcy and direct interstitial migration mechanisms, which begins with the U_i atom in a dumbbell configuration kicking out the lattice atom at the apex of the pentahedral site to the adjacent tetrahedral site, shown in Fig. 7(a) and (b). This is followed by migration of the new SIA to adjacent pentahedral and tetrahedral sites. The mechanisms for U_i migration, as observed from the bond-boost hyper-MD simulations, are demonstrated in Fig. 7. Thus, the perceived diffusion of U_i along [100], [010] and [001] crystallographic axes is a consequence of the repeated execution of the mentioned migration mechanisms. The anisotropy in the diffusivity of U_i stems from the ease of its migration via any of these mechanisms. U_i migration via the frequently observed second mechanism, as shown in Fig. 7, displaces the U_i atom along [001] and [010]. The less frequent third mechanism migrates U_i predominantly along [001], also along [010]. The first mechanism is observed in similar frequency as that of the second and it migrates U_i along [001] and [100]. Thus, the first mechanism solely drives the migration of U_i along [100].

Consequently, the computed diffusivity of U_i is highest along [001], closely followed by D_y and D_x along [010] and [100] respectively. Also, the diffusivity of U_i, computed using hyper-MD, along [100] and [010] are very close to the diffusivities reported by Wang et al. [20], as compared in Fig. 8(a), thus indicating a similar mechanism of diffusion. The diffusivity of U_i, computed using hyper-MD, along [001] slightly differs from the U_i diffusivities reported from MD studies by Wang et al. [20] specifically at low temperature. This is because at low temperature instead of migrating across the lattice, the U_i jumps back and forth between two adjacent sites for a significant part of the analyzed diffusion time. This adds to the mean squared displacement of U_i leading to an erroneous overestimate of the diffusivity. The migration energies, $E^{m}_{U_i}$, for U_i diffusion obtained from the hyper-MD runs are shown in Table 2. The migration energies reported by Wang et al. [20], computed using MD, along [100] and [010] are pretty close to the hyper-MD predictions. While the migration energy along [001] slightly differs from that reported by Wang et al. [20] by 0.09 eV.

The $E^{m}_{U_i}$ calculated from hyper-MD varies significantly from that predicted by Huang et al. [17] using first-principle calculations. This is possibly because of the difference in U_i migration mechanism observed in the hyper MD calculations and that considered by Huang et al. for their CI-NEB calculations. They only considered the migration of U_i from an initial pentahedral site to adjacent pentahedral and tetrahedral sites via interstitial mechanisms and to nearby pentahedral sites by kicking out a lattice U atom at the apex of the initial pentahedral site via an interstitialcy mechanism. However, in the hyper-MD simulations, as mentioned before and demonstrated in Fig. 7(a) and (b), we observe that a U_i, in a dumbbell configuration, kicks out the lattice U atom at the apex of the pentahedral site to the adjacent tetrahedral site. This mechanism is not considered in the CI-NEB calculations. Similarly, the migration of U_i via direct interstitial mechanism from a

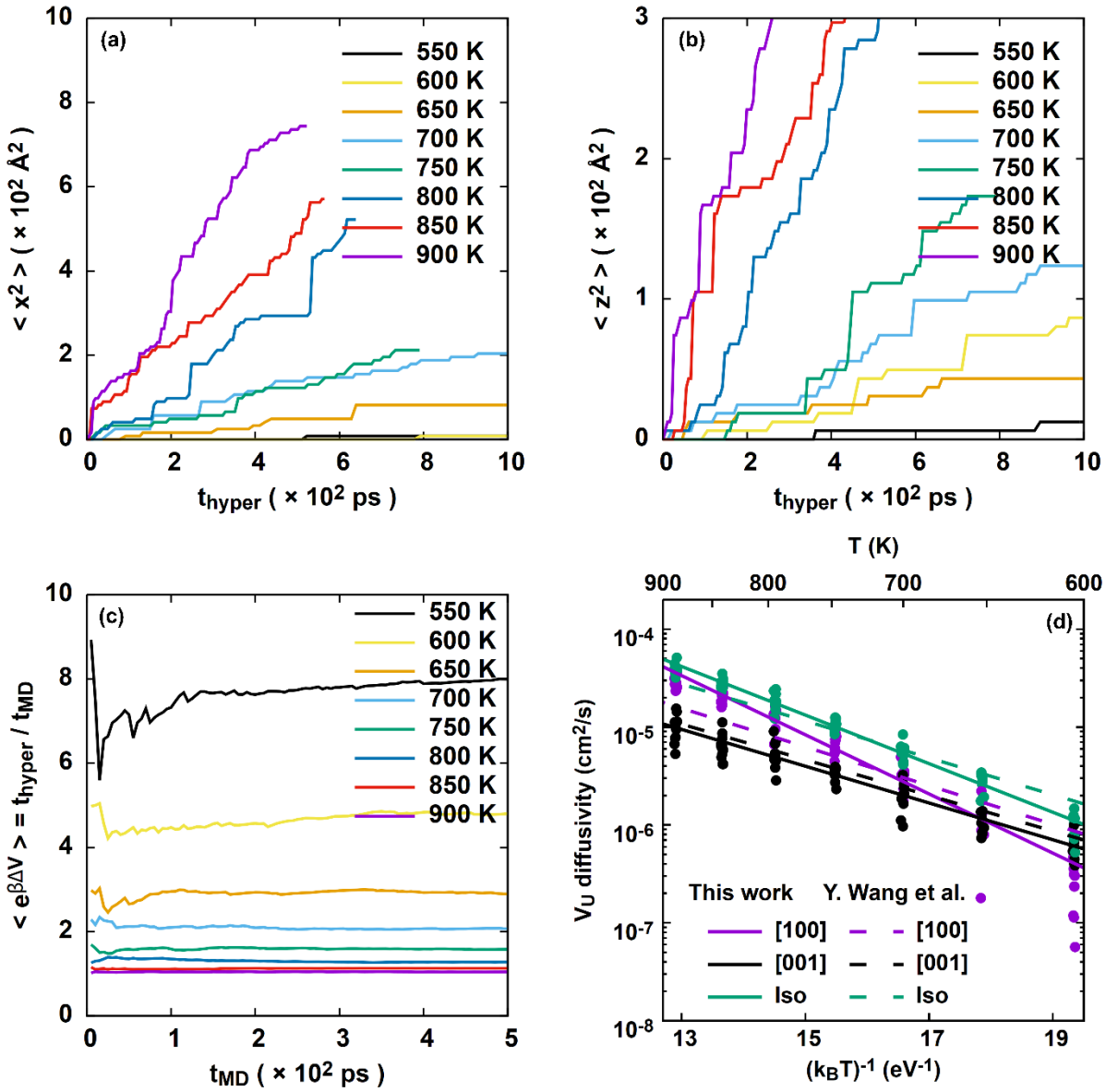

Figure 9. Mean squared displacement (MSD) plots at different temperatures for anisotropic V_U diffusion along (a) [100], (b) [001] using $\Delta V^{max} = 0.3\ eV$. (d) A comparison of the boost factors for V_U diffusion at different temperatures. (e) D_{V_U} along different crystallographic directions. The plot shows a comparison of D_x and D_z in terms of the E^m and D^o along [100] and [001] respectively. The computed diffusivity values have been compared with the diffusivity values obtained by Wang et al. [20] using MD.

tetrahedral site to adjacent pentahedral sites, observed in the first and second mechanism, has not been considered in the CI-NEB calculations. Additionally, the reason for disagreement between

the migration energies from hyper-MD and CI-NEB calculations in DFT can possibly be a consequence of the choice of interatomic potential.

3.2.3 Diffusivity of V_U

Uranium vacancies diffuse predominantly along [100] and [001] with little or no diffusion along [010] crystallographic directions. The mean squared displacement plots for V_U diffusion along [100] and [001] is shown in Fig. 9(a) and (b). The mechanisms for V_U diffusion observed in hyper-MD simulations are similar to that reported by Huang et al. [17]. A V_U in a regular lattice site of a corrugated (010) plane either jumps to its closest site along [100] or [001] during diffusion. Also, the boost potential required for diffusing V_U is smaller than the U_i, as shown in Fig. 8(c). Fig. 8(d) shows the plot of D_{V_U} along [100] and [001]. D_{V_U} along [010] could not be measured as there was no migration of V_U even at a high temperature of 900 K or a high boost potential with $\Delta V^{\max} =$ 0.4 eV. There is significant scatter in the diffusivity data at low temperature ~600 K, which reduces with the increase in temperature. D_{V_U} was observed to be slightly higher along [100] at high temperatures while its comparable with D_{V_U} along [001] at lower temperatures. Consequently, $E^{m}_{V_U}$ along [100], i.e., 0.69 eV, is higher as compared to [001], i.e., 0.43 eV. In comparison, they are 0.34 and 0.36 eV, respectively, as reported from CI-NEB calculations in DFT. Thus, the migration energy for V_U diffusion along [001] closely corresponds with the DFT calculations. Also, the diffusivity of vacancies reported by Wang et al. [20], using MD, is similar to the diffusivities predicted by hyper-MD, as shown in Fig. 8(d). The mean squared displacement plots for the point defect migration and the corresponding diffusivity plots at different values of $\Delta V^{\max}$ have been presented in the supplementary information.

4. Results from the cluster dynamics model

The calculated parameters have been used as input for our cluster dynamics (CD) model and solved using LLNL CVODE/SUNDIALS [39, 40] solver integrated with PETSc [41]. The parallel architecture of the solver used with the parallel algebraic objects of PETSc, i.e., vectors and matrices, allows significant scaling of the CD model to reach cluster sizes comparable to TEM observations, i.e., ~ 40 nm [6, 22]. As mentioned before, Hudson studied the evolution of SIA and vacancy loops on (100) and (010) planes, respectively, in neutron irradiated α-U. Using a neutron irradiation dose of 0.5 dpa at a dose-rate 4.167×10^{-7}dpa/s [6, 22, 42], the size distribution of the loops at an irradiation temperature of 80^{o}C were reported. We have used the loop size distribution measured by Hudson et al. [6] to compare the results from our CD model. The TEM micrographs of irradiated α-U shows the gradual alignment of loops, due to a glide mechanism, into near perfect rows with the increase in irradiation temperature. It is also accompanied by significant loop coarsening. At a very low temperature $\sim -196^{o}$C, the loops appear randomly distributed which start arranging into rows at $\sim 80^{o}$C on being irradiated up to 0.1 - 0.2 dpa. The mean field CD model in its present form is unable to capture the migration and patterning, i.e., arrangement into perfect rows, of the irradiation induced loops. The size distribution of loops observed at 80^{o}C and a dose of 0.5 dpa by Hudson et al. can be reasonably predicted using the mean-field CD model, as the patterning is still not significant at the mentioned irradiation dose and temperature.

Table 3. Parameters of the cluster dynamics (CD) model

Parameters	Values
Binding energy of U_i to SIA loops, $E_{U_i}^{b}$	$E_{nU_i}^{B} = E_{U_i}^{f} - a_0(n^{0.7} - (n-1)^{0.7})$ $a_0 = 4.397$ eV

Binding energy of V_U to single-layered vacancy loops, with a stacking fault, $E_{V_U}^{B}$	0.308 eV
Binding energy of V_U to double-layered vacancy loops, without a stacking fault, $E_{V_U}^{B}$	0.684 eV
Migration energy of U_i for isotropic diffusivity, $E_{U_i}^{m}$	0.34 eV
Migration energy of V_U for isotropic diffusivity, $E_{V_U}^{m}$	0.57 eV
Pre-exponential factor of isotropic U_i diffusivity, $D_{U_i}^{o}$	2.14×10^{-3} cm^2/s
Pre-exponential factor of isotropic V_U diffusivity, $D_{V_U}^{o}$	7.01×10^{-2} cm^2/s
Modified migration energy of U_i	0.25 eV
Formation energy of U_i, $E_{U_i}^{f}$	4.42 eV [17]
Formation energy of V_U, $E_{V_U}^{f}$	1.69 eV [17]

4.1 Experimental conditions and input parameters

Similar to the neutron irradiation experiments [6], the conditions chosen as input for our CD model are an irradiation temperature of 80^{o}C and a dose-rate of 4.167×10^{-7}dpa/s. The choice of parameters for the model is critical to accurately predict the loop densities at any given irradiation condition. We have used the parameters computed in the previous section, i.e., the binding energy of point defects to clusters and the mobility of point defects, as listed in Table 3. The migration energies of U_i, computed assuming isotropic diffusion, i.e., 0.34 eV, as shown in Table 2, has been slightly modified to 0.25 eV to obtain the closest fit of the size distribution plot of loops with the TEM observations. The predictions from our CD model and its comparison to the loop size distribution, reported by Hudson [6], is shown in Fig. 10. The modified migration energy of U_i is justified owing to the error in the diffusivity, computed using bond-boost hyperdynamics, as shown in Fig. 8(e). This provides us a window of uncertainty, within which $E_{U_i}^{m}$ can be systematically varied to obtain a good fit of the CD predictions with the TEM observations. The binding energy of respective point defects to the SIA and vacancy loops depend on the type of loop, i.e., with or without an associated stacking fault. As discussed in Section 2.1, the vacancy loops can either exist as a single layered loop with an associated stacking fault or a double layered loop without a stacking fault. We have also seen in Section 3.1 that a larger positive value of the binding energy,

$E_{V_U}^{B}$, of double layered vacancy loops render them more stable as compared to their single layered counterparts in irradiated α-U. This plays a significant role in the evolution of vacancy loops, of a particular type, on irradiation.

4.2 Predictions from the CD model and comparison with TEM observations

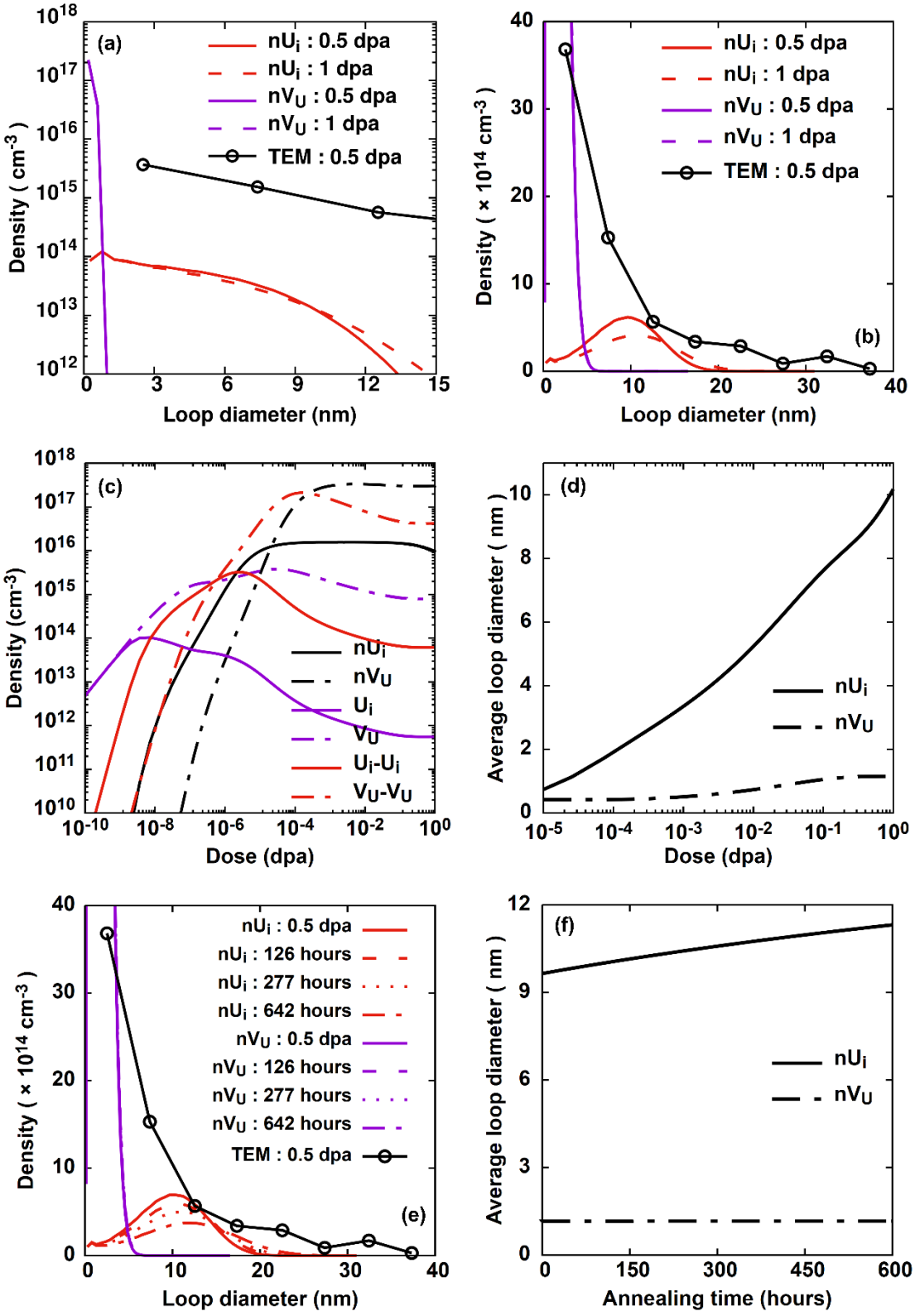

Figure 10. (a) CD predicted evolution of the size distribution plot (SDF) of SIA and single-layered vacancy loops with a dose-rate of 4.2×10^{-7} dpa/s at $80^{o}C$. The index for the plot is given in (b) where nU_i and nV_U indicates SIA and vacancy loops respectively. Inset shows the density of loops, using a log axis. The TEM observed loop densities is obtained from the work by Hudson et al. [6]. (b) CD predicted SDF of SIA and double-layered vacancy loops. (c) The evolution of the density of monomers, i.e., U_i and V_U, dimers, i.e., $U_i - U_i$ and $V_U - V_U$, and SIA and vacancy loops with irradiation dose. (d) CD predicted SIA and vacancy loop size evolution with dose. CD predicted (e) SDF and (f) the variation of average loop diameter of the SIA and vacancy loops calculated during annealing at $80^{o}C$ after an irradiation upto a dose of 0.5 dpa.

Fig. 10(a) and (b) shows the CD predicted size distribution of SIA and vacancy loops. The loop densities obtained by Hudson et al. from the TEM observation of α-U, neutron-irradiated up to 0.5 dpa at 80ºC, has been rescaled by a factor of 10 based on the ratio of histogram bin sizes chosen for the experiments, i.e., 50 Å, and the CD simulations, i.e., 5 Å. It is important to mention that the TEM investigation reported a total density of SIA and vacancy loops due to the difficulty in distinguishing them separately. Fig. 10(a) shows the CD predicted size distribution of SIA and single layered vacancy loops on being irradiated at 80ºC. We observe an accumulation of very small sized vacancy loops, along with a distribution of SIA loop densities over a range of sizes. With the progress of irradiation, the accumulated density of vacancy loops remain unchanged whereas the SIA loops exhibit growth, as the size distribution plot shift to larger loop sizes with a slight depletion of peak loop density, shown in the inset of Fig. 10(a). However, the TEM observed loop densities are nearly two orders of magnitude higher than the CD predictions, as compared in the inset of Fig. 10(a), at an irradiation dose of 0.5 dpa. Also, the density of larger loops with size > 20 nm are negligibly insignificant compared to the density of such loops reported in the TEM observations.

Fig. 10(b) shows the CD predicted evolution of loop densities, considering SIA and double layered vacancy loops in the irradiated matrix. We see a significant difference in size distribution of SIA and vacancy loops as compared to Fig. 10(a). Though there is an accumulation of small sized double-layered vacancy loops, the size range of such loops is ~ 10 nm which is considerably

higher than the small single-layered vacancy loops in Fig. 10(a). The high density of small double-layered vacancy loops is nearly two orders of magnitude higher than the density of larger SIA loops with size ≥ 7 nm. On the other hand, the density of small loops observed in TEM, is about eight times higher than the density of large loops. The high density of small vacancy loops, predicted using CD, is likely to remain unresolved in TEM due to their sub-nanometric sizes. Thus, the TEM observations only reported an eight times higher density than the large loops while CD predicts a difference in two orders of magnitude. Also, the size distribution of SIA loops is spread over significantly higher loop size ranges with densities comparable to that reported for larger loops of size ≥ 7 nm, from the TEM observations by Hudson et al [6].

This marked difference in the CD predictions with single and double-layered vacancy loops is predominantly attributed to the stability of each loop. The binding energy of vacancies being higher for double-layered vacancy loops make them more stable. Consequently, they shrink at a considerably lower rate by emitting vacancies as compared to the single-layered loops. This allows the growth of relatively larger vacancy loops, seen as a spread of the size distribution plot over a range of loop sizes, with densities roughly comparable to the TEM observed loop densities. The high rate of vacancy emission from single-layered loops enhances the absorption of vacancies by SIA loops, restricting their growth significantly. Thus, the CD predictions in Fig. 10(a) shows a difference in the SIA loop densities with the TEM observed loop densities by almost two orders of magnitude.

Fig. 10(c) shows the density variation of point defects and SIA and vacancy loops with irradiation dose. As irradiation begins, Frenkel pairs generate in the matrix resulting in the accumulation of U_i and V_U in equal density. This is followed by the initiation of U_i-U_i SIA dimers with the progress of irradiation. U_i being more mobile than V_U, migrates easily and starts forming dimers and small

SIA clusters. Migration and recombination of U_i and V_U takes place continuously in the irradiated α-U matrix. As a result, the U_i density starts depleting with a continued accumulation of V_U. Eventually, the rate of V_U accumulation slows down as the generation of V_U-V_U dimers begin on further irradiation. This coincides with the initiation of SIA loop generation which absorbs U_i and V_U from the irradiated matrix, further depleting the U_i density and slowing down the rate of V_U accumulation. As the dose increases further, vacancy loops start generating which leads to a depletion of V_U density and continued absorption of U_i from the matrix. The dimers and small clusters progressively grow into large loops eventually saturating their density. Fig. 10(d) clearly shows the growth of SIA loops as the average loop size consistently keep increasing with dose. The growth of SIA loops is also observed in Fig. 10(b) where the size distribution plot shifts to larger loop sizes with irradiation. However, the vacancy loops do not grow significantly on irradiation as we observe a negligible increase in the average size, on irradiation up to 1 dpa. The size distribution plot of vacancy loops in Fig. 10(b) shows a huge accumulation of small vacancy loops, which does not change significantly on irradiation even at high doses further indicating extremely slow growth of loops. This is primarily due to the sluggish kinetics of U vacancies.

4.3 Coarsening of loops at high dose and during post-irradiation annealing

The CD simulations considering SIA and double-layered vacancy loops closely predicts the density of point defect loops similar to the TEM observations by Hudson et al., assuming that the high density of small loops are predominantly of vacancy type whereas the large loops are of SIA type. However, at an irradiation dose of 0.5 dpa the CD predicted density of large loops, with size > 20 nm, is still significantly lower than the TEM observations by at least a factor of 5. This discrepancy can be attributed to the mechanism of loop migration and coalescence, due to elastic interactions, leading to extensive coarsening as reported by Hudson et al. The CD model in its

present form does not consider loop growth due to coalescence with other loops. It only consider the point defects, i.e., U_i and V_U, to be the mobile defect species which gets absorbed by the immobile loops. In order to represent the growth of large SIA loops, we have run the CD simulations up to an irradiation dose of 1 dpa. The size distribution of SIA loops at an irradiation dose of 1 dpa has been shown in Fig. 10(b). We see an observable growth of loops indicated by the spread of size distribution plots to larger loop sizes. Additionally, we also have performed CD simulations of annealing the α-U matrix after irradiating it to 0.5 dpa at 80^{o}C. This is done by systematically stopping the generation of Frenkel pairs in the CD equations, represented as $G_{1\mathrm{i}}$ and $G_{1\mathrm{v}}$ in Eq. (5) and (6) respectively, after an irradiation dose of 0.5 dpa is reached. It is followed by allowing the irradiated matrix with point defects and loops to evolve for a prolonged period. A similar treatment of post-irradiation annealing in irradiated ThO_2, using CD, has been recently demonstrated by S. K. Mazumder et al. [43]. The size distribution plots for post-irradiation annealing of irradiated α-U, predicted using CD, has been presented in Fig. 10(e). We observe that with the progress of annealing, the SIA loops continue growing and almost reaches the size and density of large loops > 20 nm reported in the TEM observations. The growth of SIA loops during annealing is also apparent from the monotonous increase of the average loop size with annealing time, as shown in Fig. 10(f). However, the vacancy loops do not show any observable growth mechanism due to which their average size remains constant during the entire annealing period. This is a consequence of the sluggish V_U kinetics which restricts the growth of small vacancy loops significantly.

4.4 Evolution of loops on irradiation at a high temperature

Irradiation at a higher temperature accelerates the rate of point defect recombination in the matrix which significantly slows down the growth of loops. The CD predicted size distribution plot of SIA and double-layered vacancy loops on irradiation at 160°C up to a dose of 0.1 dpa has been

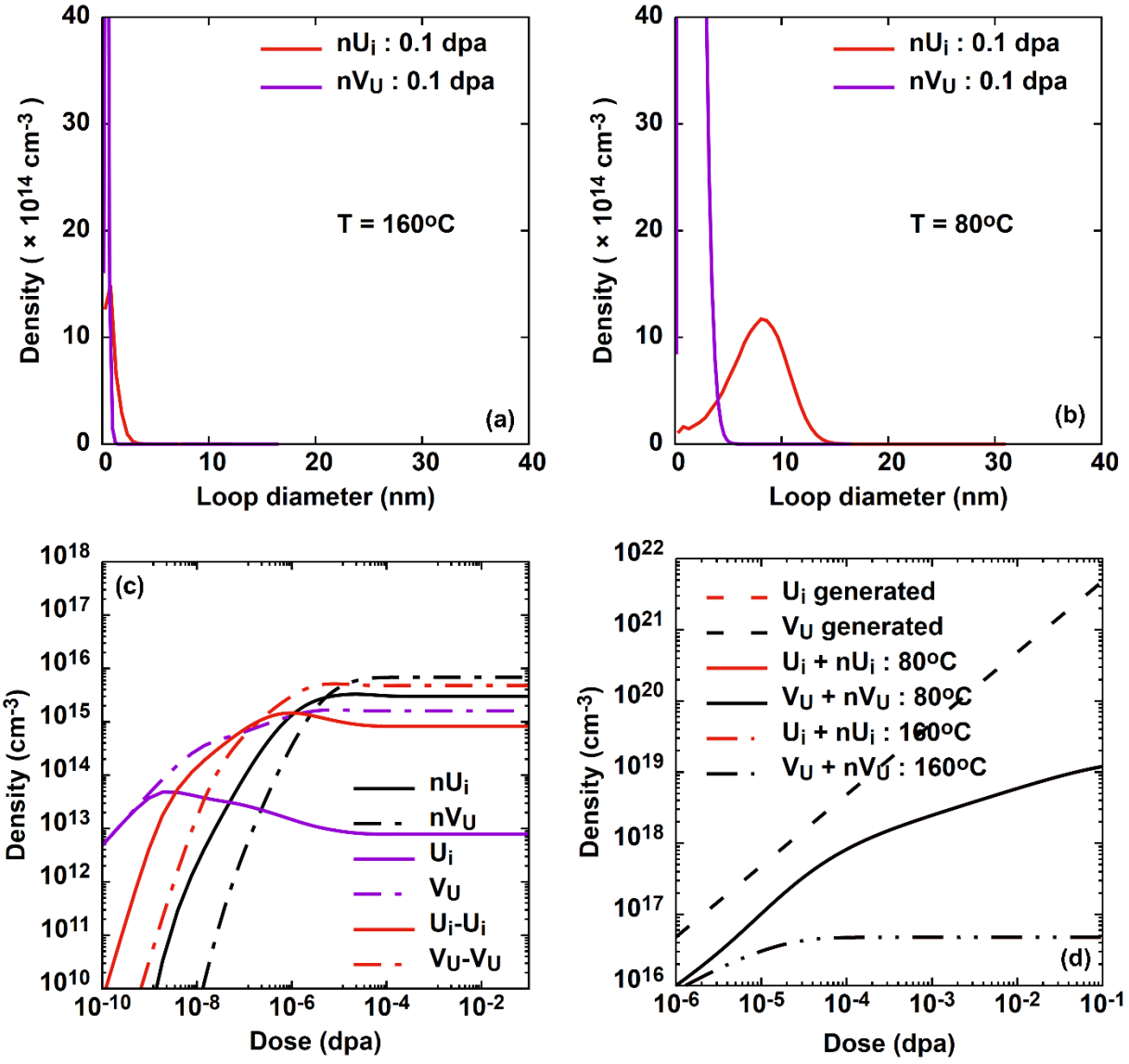

Figure 11. Size distribution plot of SIA and vacancy loops on irradiation at (a) 160°C and (b) 80°C, upto 0.1 dpa with a dose-rate of 4.2×10^{-7} dpa/s. (c) Evolution of the density of monomers, i.e., U_i and V_U, dimers, i.e., $U_i - U_i$ and $V_U - V_U$, and SIA and vacancy loops with irradiation dose at 160°C. (d) Density of U_i and V_U which generates as Frenkel pairs in the displacement cascade and the total density that exist as monomers and clustered in SIA and vacancy loops in the matrix.

presented in Fig. 11(a). When compared with the size distribution plot of loops irradiated up to 0.1 dpa at 80^{o}C, as shown in Fig. 11(b), we observe that there is an accumulation of very small loops, whose growth is severely restricted. The total density of small SIA and vacancy loops saturates with dose as shown in Fig. 11(c). The saturated total concentration of SIA loops, i.e., predominantly small loops, are almost an order of magnitude and the small vacancy loops are almost two orders of magnitude lower than that observed in Fig. 10(c). This is a consequence of the accelerated recombination of point defects due to enhanced mobility at high temperatures. The effects of enhanced recombination have been demonstrated by accounting for the total number of point defects generated as Frenkel pairs in the cascade and that clustered in dimers and loops on irradiation. The density of U_i and V_U generated in the cascade is the same due to their existence as Frenkel pairs. This is represented with a broken line, as shown in Fig. 11(d), which keeps linearly increasing with a constant dose rate 4.2×10^{-7} dpa/s. The total density of U_i and V_U which exist as monomers and clustered in dimers and loops in the irradiated matrix shows a deviation from the linear behaviour with irradiation dose. The difference in the density of monomers generated in the cascade and that which exist as monomers and clusters in the irradiated matrix, equals the density of monomers that recombined. As the point defects can annihilate only via recombination, the total density of U_i and V_U that exist as monomers and clustered in SIA and vacancy loops should also overlap in Fig. 11(d). Since the recombination of point defects is driven by their diffusion towards

each other, as shown in Eq. 7, the density of annihilated monomers due to recombination increases significantly on increasing irradiation temperature. As a consequence, the density of monomers available for clustering depletes, which in turn reduces the density of small SIA and vacancy loops that form in the matrix.

4.5 Comparison of CD predictions for different point defect diffusivities

As mentioned in Section 3.1, the CD model is sensitive to the migration energy of point defects which govern the defect clustering kinetics. An accurate choice of migration energies for the model is motivated by a good prediction of the TEM observed size distribution plot of loops, reported by Hudson et al. [6] We tested the diffusivity of point defects computed using hyper-MD simulations, in this work, as well as the values reported by the recent work of Wang et al. [20], listed in Table 2. CD predictions corresponding to both the diffusivity data are presented in Fig. 12(a) and (b) respectively. The pre-exponential diffusivity values, though important, does not significantly influence the CD predictions as the point defect migration energies. In Fig. 12(a) and (b), the size

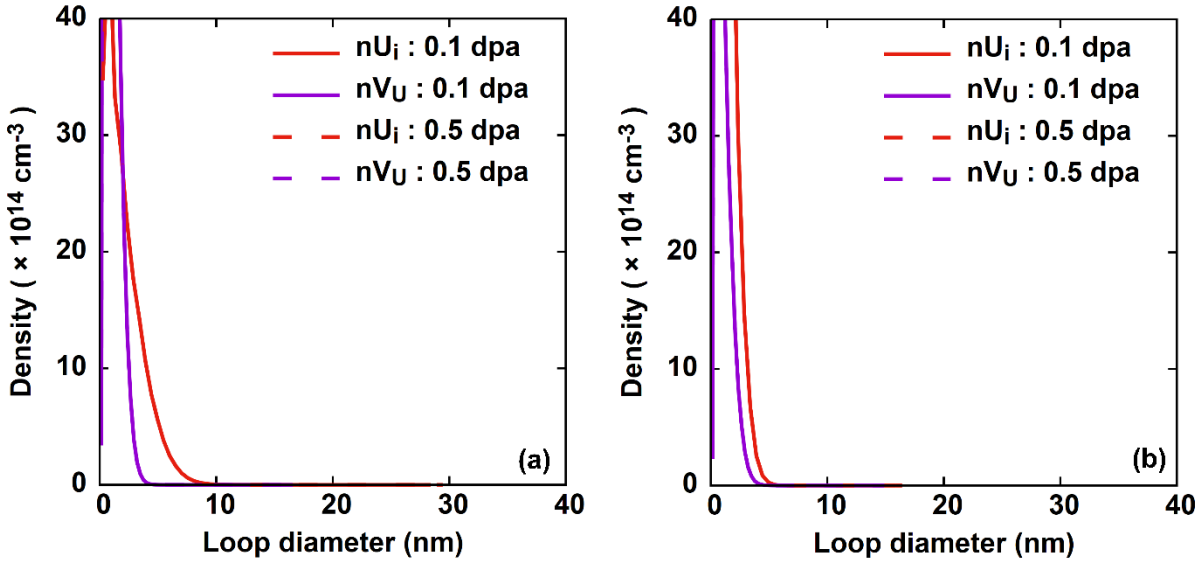

Figure 12. CD predicted size distribution plot of SIA and vacancies loops, on irradiation with a similar dose-rate of 4.2×10^{-7} dpa/s at 80°C, using the point defect diffusivities given by (a) hyperdynamics simulations presented in this work and (b) Wang et al. [20] listed in Table 2.

distribution plots show a huge accumulation of very small sized SIA and vacancy loops which does not exhibit growth, even at a high irradiation dose. This is possibly because of the low U_i mobilities with $E_{U_i}^m = 0.34$ and 0.42 eV predicted by hyper-MD and Wang et al. [20], respectively. Thus, choosing a lower $E_{U_i}^m \sim 0.25$ eV allows the SIA loops to grow significantly. Error in the hyper-MD computed $E_{U_i}^m$, due to the spread in diffusivities shown in Fig. 8(e), allows us to vary it within a window of uncertainty $\sim$1 eV and choose a value that predicts the TEM observed SIA loop distribution closely. We also acknowledge the limitation in the CD model, considering only the mobility and interaction of point defects, due to which it is hard to accurately predict the TEM observed large loop densities. On the other hand, as discussed in Section 3.1, the vacancy loops do not show extensive growth even when $E_{V_U}^m$ is slightly modified within a window of uncertainty $\sim$1 eV. Thus, the small sized loops predicted by the CD model are predominantly vacancy type, whereas the larger loops are SIA type. A list of size distribution plots obtained using a range of diffusivity values is presented in the supplementary material.

5. Discussion

5.1 Crystallography of point defect loops

In this work, we have discussed the crystallography of defect loops observed in neutron irradiated α-U in detail. The habit planes and Burgers vector of both kind of loops have been determined by Hudson [6, 22] from the TEM observations of neutron irradiated α-U. The SIA loops form a stacking fault between the (010) planes of α-U whereas the vacancy loops can either exist with or without a stacking fault depending on whether the vacancies condense on a single (100) plane or two consecutive (100) planes. Similar configuration of SIA loops have previously been discussed by Li et al. [44]. However, a detailed analysis of the U_i sites in the α-U lattice has not been

presented before. Similarly, a detailed description of the vacancy loop configuration has been missing in the literature. A comprehensive understanding of the loop crystallography helps us compute their energetics and further study their evolution, using cluster dynamics, under irradiation. It is important to mention here that the motivation behind creating the loops in a particular crystallographic arrangement solely relies on the TEM observations by Hudson. Defect loops with different habit planes and Burgers vectors, leading to the dimensional instability, can also be studied similarly if their presence in the irradiated matrix is reported from detailed TEM investigation. Recent *in-situ* studies by Di Lemma et al. [45] also reported the formation of {130} loops during *in-situ* TEM pure heating of α-U previously irradiated in Transient Reactor Test Facility to 0.08-0.371 MWd/MTU. The discrepancy indicates possibly different defect reorganization mechanism between pure thermal and coupled thermal irradiation conditions.

5.2 Diffusivity of point defects

The bond-boost hyperdynamics method have been implemented to study the diffusivity of individual point defects over long timescales ~ 1 μs at temperatures below 935 K, the $\alpha \rightarrow \beta$ transformation temperature. Wang et al. [20] recently reported the point defect diffusivities, using the angular dependent EAM potential by Starikov et al. [19] in MD, the migration energies of which largely vary from the previous MD calculations by Beeler et al. [18] and CI-NEB calculations in DFT by Huang et al. [17] Also, a detailed analysis of the point defect migration mechanisms leading to any observed anisotropy in the hyperdynamics simulations have been presented. The migration of SIA is almost isotropic at high temperatures, with the diffusivities along three directions varying within a window of less than an order of magnitude, as shown in Fig. 8(e). The anisotropic behaviour of diffusion becomes significant at low temperature which can be attributed to the activation energies associated with the different migration mechanisms

demonstrated in Fig. 7. Both of the frequently observed second and first mechanisms migrate U_i along [001]. On the other hand, U_i migrates along [010] and [100] only via second and first mechanisms respectively. At low temperatures, both mechanisms are not properly active which results in a limited migration of U_i. However, the third mechanism is still observed at low temperature which relatively increases U_i migration along [001]. The diffusivities at low temperatures are also overpredicted due to a continuous back and forth jumping of U_i between adjacent sites. The anisotropy observed in the migration of V_U is significantly larger than that of U_i as predicted in [15, 16, 17]. The migration of V_U predominantly takes place along [100] and [010] in the (010) corrugated planes, even at high temperatures. The in-plane diffusion of V_U is not biased along any direction. Thus, we do not observe any preferable diffusion of U_i along [010] and V_U along [100], as proposed by Siegle and Opinsky [3] for the dimensional instability in α-U, under irradiation.

5.3 Evolution of defect loops predicted using CD

The mean field cluster dynamics (CD) model presented in this work closely predicts the size distribution plot of defect loops observed in neutron-irradiated α-U at 80^{o}C [6]. As discussed in Section 3.4, the point defect diffusivities govern the kinetics of the clustering phenomenon and hence, the evolution of loops at different irradiation doses and temperature. The diffusivity of U_i and V_U, along the different crystallographic directions, computed using hyper-MD is very similar to the predictions from temperature accelerated MD by Wang et al. [20] The migration energy of U_i, reported in this work, has been slightly varied over a window of uncertainty $\sim$1 eV, based on the spread of the U_i diffusivity values, as shown in Fig. 8(e). Using the modified migration energy of U_i, shown in Table 3, CD closely predicts the TEM observed loop size distribution as shown in Fig. 10(b). The predicted density of loops, with size $\sim 10-20$ nm, is slightly smaller than the

TEM observations, as shown in Fig. 10(b) and discussed in Section 4.2 and 4.3. Loop density measured in the TEM samples is likely to be overestimated than the bulk microstructure, due to the defects introduced during TEM sample milling. The modified $E_{\mathrm{U_i}}^{\mathrm{m}}$ is close to the CI-NEB calculations in DFT by Huang et al. [17] In order to further improve the choice of point defect diffusivities for a better prediction of defect cluster population, we need more experimental studies on irradiated α-U. There exists limited literature on the measurement of defect evolution in α-U under irradiation which has resulted in the investigations by Hudson et al. being the only reliable source of experimental observations required for the validation of our CD model. Also, as already mentioned in Section 3.2, the CD model in its present form is not informed with the physics of loop coarsening due to migration and coalescence which is also a significant source of error for loop density predictions in the large size ranges, especially at irradiation temperatures $\sim 100^{\mathrm{o}}\mathrm{C}$. Nonetheless, it is a powerful technique that can be reliably utilized to predict defect accumulation at low irradiation temperatures as a first step towards estimating dimensional instability in irradiated α-U. Further improvements in the model are underway to incorporate the physics behind loop coarsening driven by coalescence, observed at high temperatures. Additionally, the CD model predicts the nature of vacancy loops that are likely to exist in the neutron-irradiated microstructure. Double layered loops being energetically more stable should be predominant in the matrix. Thus, a detailed characterization of the irradiation induced loops using TEM would further help in verifying this prediction.

6. Summary and conclusions

We have presented an atomistically informed mean field cluster dynamics model to predict the evolution of point defect clusters in irradiated α-U at different temperature ranges. Though neutron irradiated α-U shows organization of such loops at high irradiation temperatures, a mean field CD

model can be reasonably used to predict mean density of loops and their size distribution in the intermediate temperature ranges, i.e., $\sim 80^{o}C$, at which patterning of loops, in the microstructure, due to migration and rearrangement is not prevalent. A detailed analysis has been presented on the crystallography of SIA and vacancy loops on (010) and (100) planes respectively. The U_i in an SIA loop occupies the pentahedral interstitial sites in between the corrugated (010) planes in α-U. On the other hand, the vacancy loops exist on the (100) planes and can either be single layered loops with a stacking fault or a double layered loop without a stacking fault. Stability of the SIA and vacancy loops have been determined by computing the energy associated with the binding of point defects to the loops, using the angular dependent EAM potential by Starikov et al. [19]. The SIA loops become more stable with an increase in size. Similarly, the double layered vacancy loops are found to be more stable as compared to the single layered loops. Energy associated with the stacking fault increases the formation energy of single layered vacancy loops. The diffusivities of U_i and V_U have been studied using bond-boost hyperdynamics in LAMMPS. The anisotropy of V_U migration is significant, as the diffusion of V_U could only be observed on (010) corrugated planes. U_i migration shows anisotropy to some extent which is a consequence of their migration mechanism observed in the hyperdynamics simulations. Our diffusivity data corresponds closely with the classical MD calculations recently reported by Wang et al. [20] with little discrepancies on the evaluated migration energies of point defects along specific crystallographic directions. The detailed mechanism of U_i migration has also been presented in this work. However, we have used an isotropic diffusivity of the point defects for our mean field CD model.

CD predictions using the computed point defect diffusivities show an accumulation of small sized SIA and vacancy loops without any significant growth of the small loops even at high irradiation doses. The modified migration energy of U_i diffusion leads to the growth of SIA loops significantly

which fits closely with the reported size distribution of loops in neutron irradiated α-U by Hudson et al. The small sized vacancy clusters still accumulate in the matrix significantly with dose, fitting the TEM observed size distribution of loops in the small size regime. Further analysis of defect cluster evolution on irradiation at a high temperature and during post-irradiation annealing has also been presented. The CD model is not capable of predicting extensive loop coarsening observed by Hudson et al. [6, 22] due to an absence of the physics behind migration and interaction between loops leading to coalescence. However, it is still an efficient model to obtain a good estimate of defect population in irradiated fuels, like α-U, especially in the low and intermediate irradiation temperature ranges and low irradiation doses, where coarsening due to coalescence is not expected to be significant. The density of accumulated SIA and vacancy loops, predicted from the CD model, can further be used to estimate the extent of anisotropic swelling in irradiated α-U.

Conflict of interest

There are no conflicts to declare.

Acknowledgements

This work was supported by Center for Thermal Energy Transport under Irradiation, an Energy Frontier Research Center funded by the U.S. Department of Energy, Office of Science, Office of Basic Energy Sciences. We would like to acknowledge the valuable inputs from Tomohisa Kumagai from Central Research Institute of Electric Power Industry (CRIEPI), Yokosuka, Kanagawa, 2400196, Japan on the hyperdynamics calculations of point defect diffusivity using LAMMPS.

References

[1] A. Seshadri, A. M. Jokisaari, C. Sun, A Review of Irradiation Damage and Effects in α-Uranium, Materials 15 (2022) 4106.

[2] S. H. Paine, J. H. Kittel, Preliminary Analysis of Fission-Induced Dimensional Changes in Single Crystals of Uranium, ANL-5676, Argonne National Lab, Lemont, IL, USA, 1958.

[3] L. L. Seigle, A. J. Opinsky, Mechanism of Dimensional Instability of Uranium, Nucl. Sci. Eng. 2 (1957) 38-48.

[4] F. R. N. Nabarro, Report of the Conference on the Strength of Solids, Physical Society, London, 1948, 75.

[5] S. Buckley, Proceedings of the International Conference, Berkeley Castle, Gloucestershire, UK, 1961.

[6] B. Hudson, K. H. Westmacott, M. J. Makin, Dislocation loops and irradiation growth in alpha uranium, Philos. Mag. 7 (1962) 377-392.

[7] L. K. Mansur, Theory and experimental background on dimensional changes in irradiated alloys, J. Nucl. Mater. 216 (1994) 97-123.

[8] A. H. Duparc, C. Moingeon, N. Smetniansky-De-Grande, A. Barbu, Microstructure modelling of ferritic alloys under high flux 1 MeV electron irradiations, J. Nucl. Mater. 302 (2022) 143-155.

[9] A. Gokhman, F. Bergner, Cluster dynamics simulation of point defect clusters in neutron irradiated pure iron, Radiat. Eff. Defects Solids 165 (2010) 216-226.

[10] C. Pokor, Y. Brechet, P. Dubuisson, J. P. Massoud, A. Barbu, Irradiation damage in 304 and 316 stainless steels: experimental investigation and modeling. Part I: Evolution of the

microstructure, J. Nucl. Mater. 326 (2004) 19-29.

[11] D. Brimbal, L. Fournier, A. Barbu, Cluster dynamics modeling of the effect of high dose irradiation and helium on the microstructure of austenitic stainless steels, J. Nucl. Mater. 468 (2016) 124-139.

[12] F. Christien, A. Barbu, Effect of self-interstitial diffusion anisotropy in electron-irradiated zirconium: A cluster dynamics modeling, J. Nucl. Mater. 346 (2005) 272-281.

[13] S. K. Mazumder, M. K. S. Singh, T. Kumagai, A. El-Azab, Atomistically-informed modeling of point defect clustering and evolution in irradiated ThO_2, Chem. Phys. 562 (2022) 111645.

[14] S. Khalil, T. Allen, A. El-Azab, Off-stoichiometric defect clustering in irradiated oxides, Chem. Phys. 487 (2017) 1-10.

[15] A. A. Bochvar, V. G. Kuznetsova, V. S. Sergeev, F. P. Butra, Atomnaya Energiya, 1965, 18, 601–608.

[16] S. J. Rothman, J. J. Hines, J. Gray, Jr, A. L. Harkness, Anisotropy of Self-Diffusion in Alpha Uranium, J. Appl. Phys. 33 (1962) 2113-2116.

[17] G-Y. Huang, B. D. Wirth, First-principles study of diffuison of interstitial and vacancy in α U-Zr, J. Phys. Condens. Matter 23 (2011) 205402.

[18] B. Beeler, Y. Zhang, M. Okuniewski, C. Deo, Calculation of the displacement energy of α and γ uranium, J. Nucl. Mater. 508 (2018) 181-194.

[19] S. V. Starikov, L. N. Kolotova, A. Yu. Kuksin, D. E. Smirnova, V. I. Tseplyaev, Atomistic simulation of cubic and tetragonal phases of U-Mo alloy: Structure and thermodynamic properties, J. Nucl. Mater. 499 (2018) 451-463.

[20] Y. Wang, B. Beeler, A. Jokisaari, An atomistic study of fundamental bulk and defect properties in α-uranium, J. Nucl. Mater. 576 (2023) 154289.

[21] C. S. Barrett, M. H. Mueller, R. L. Hitterman, Crystal Structure Variations in Alpha Uranium at Low Temperatures, Phys. Rev. 129 (1963) 625-629.

[22] B. Hudson, The crystallography and burgers vectors of dislocation loops in α-uranium, Philos. Mag. 10 (1964) 949-960.

[23] D. E. Smirnova, A. Yu. Kuksin, S. V. Starikov, Investigation of point defects diffusion in bcc uranium and U-Mo alloys, J. Nucl. Mater. 458 (2015) 304-311.

[24] D. E. Smirnova, S. V. Starikov, V. V. Stegailov, Interatomic potential for uranium in a wide range of pressures and temperatures, J. Phys.: Condens. Matter 24 (2012) 149501.

[25] B. Beeler, B. Good, S. Rashkeev, C. Deo, M. Baskes, M. Okuniewski, First-principles calculations of the stability and incorporation of helium, xenon and krypton in uranium, J. Nucl. Mater. 425 (2012) 2-7.

[26] B. Beeler, B. Good, S. Rashkeev, C. Deo, M. Baskes, M. Okuniewski, First principles calculations for defects in U, J. Phys.: Condens. Matter 22 (2010) 505703.

[27] C. D. Taylor, Evaluation of first-principles techniques for obtaining materials parameters of α-uranium and the (001) α-uranium surface, Phys. Rev. B 77 (2008) 094119.

[28] B. Beeler, K. Mahbuba, Y. Wang, A. Jokisaari, Determination of Thermal Expansion, Defect Formation Energy and Defect-Induced Strain of α-U Via *ab Initio* Molecular Dynamics, Front. Mater. 8 (2021) 661387.

[29] N. Soneda, T. Diaz De La Rubia, Defect production, annealing kinetics and damage evolution

in α-Fe: An atomic-scale computer simulation, Philos. Mag. A 78 (1998) 995-1019.

[30] M. R. Sørensen, A. F. Voter, Temperature-accelerated dynamics for simulation of infrequent events, J. Chem. Phys. 112 (2000) 9599.

[31] F. Montalenti, M. R. Sørensen, A. F. Voter, Phys. Rev. Lett. 87 (2001) 126101.

[32] R. A. Miron, K. A. Fichthorn, Accelerated molecular dynamics with the bond-boost method, J. Chem. Phys. 119 (2003) 6210-6216.

[33] A. F. Voter, A method for accelerating the molecular dynamics simulation of infrequent events, J. Chem. Phys. 106 (1997) 4665-4667.

[34] A. F. Voter, Hyperdynamics: Accelerated Molecular Dynamics of Infrequent Events, Phys. Rev. Lett. 78 (1997) 3908-3911.

[35] A. F. Voter, Parallel replica method for dynamics of infrequent events, Phys. Rev. B 57 (1998) 13985-13988.

[36] C-S. Yoo, H. Cynn, P. Söderlind, Phase diagram of uranium at high pressures and temperatures, Phys. Rev. B 57 (1998) 10359.

[37] S. Y. Kim, D. Perez, A. F. Voter, Local hyperdynamics, J. Chem. Phys. 139 (2013) 144110.

[38] A. Stukowski, Visualization and analysis of atomistic simulation data with OVITO-the Open Visualization Tool, Model. Simul. Mater. Sci. Eng. 18 (2009) 015012.

[39] S. D. Cohen, A. C. Hindmarsh, P. F. Dubois, A Stiff/Nonstiff ODE Solver in C, Computers in Physics 10 (1996) 138-143.

[40] R. Serban, A. C. Hindmarsh, CVODES: The Sensitivity-Enabled ODE Solver in SUNDIALS,

Proceedings of IDETC/CIE, DETC2005-85597, 2005.

[41] S. Abhyankar, J. Brown, E. M. Constantinescu, D. Ghosh, B. F. Smith, H. Zhang, PETSc/TS: A Modern Scalable ODE/DAE Solver Library, Arxiv preprint arXiv:1806.01437v1, 2018.

[42] R. J. McElroy, Irradiation growth during fission fragment and proton bombardment of uranium, J. Nucl. Mater. 90 (1980) 297-306.

[43] S. K. Mazumder, K. Bawane, J. M. Mann, A. French, L. Shao, L. He, A. El-Azab, Evolution of dislocation loops and voids in post-irradiation annealed ThO_2: A combined *in-situ* TEM and cluster dynamics investigation, J. Nucl. Mater. preprint NUMA 154686, https://doi.org/10.1016/j.jnucmat.2023.154686, 2023.

[44] Y. Li, A. Chernatynskiy, J. R. Kennedy, S. B. Sinnott, S. R. Phillpot, Lattice expansion by intrinsic defects in uranium by molecular dynamics simulation, J. Nucl. Mater. 475 (2016) 6-18.

[45] F. G. Di Lemma, T. Yao, D. Salvato, L. Capriotti, F. Teng, A. M. Jokisaari, B. W. Beeler, Y. Wang, C. J. Jensen, Microstructural and phase changes in alpha uranium investigated via *in-situ* studies and molecular dynamics, J. Nucl. Mater. 577 (2023) 154341.

[46] R. A. Johnson, Calculations for the stability of voids, stacking-fault tetrahedra, and dislocation loops in nickel, Philos. Mag. 16 (1967) 553-564.

[47] A. O. Thompson, H. M. Aktulga, R. Berger, D. S. Bolintineanu, W. M. Brown, P. S. Crozier, P. J. in ‘t Veld, A. Kohlmeyer, S. G. Moore, T. D. Nguyen, R. Shan, M. J. Stevens, J. Tranchida, C. Trott, S. J. Plimpton, LAMMPS – a flexible simulation tool for particles based materials modeling at the atomic, meso, and continuum scales, Comput. Phys. Commun. 271 (2022) 108171.

[48] X. -Y. Liu, C. Matthews, W. Jiang, M. W. D. Cooper, J. D. Hales, D. A. Andersson, Atomistic

and cluster dynamics modeling of fission gas (Xe) diffusivity in TRISO fuel kernels, J. Nucl. Mater. 561 (2022) 153539.

[49] C. Matthews, R. Perriot, M. W. D. Cooper, C. R. Stanek and D. A. Andersson, Cluster dynamics simulation of xenon diffusion during irradiation in UO_2, J. Nucl. Mater. 540 (2020) 152326.

[50] C. Matthews, R. Perriot, M. W. D. Cooper, C. R. Stanek and D. A. Andersson, Cluster dynamics simulation of uranium self-diffusion during irradiation in UO_2, J. Nucl. Mater. 527 (2019) 151787.